The Pennsylvania State University
The Graduate School
Department of Mechanical Engineering

CORRELATED-*k* DISTRIBUTION METHOD FOR SOLVING ATOMIC RADIATION PROBLEM IN HYPERSONIC NONEQUILIBRIUM FLOWS

A Thesis in
Mechanical Engineering
by
Ankit Bansal

Submitted in Partial Fulfillment
of the Requirements
for the Degree of

Master of Science

August 2009

The thesis of Ankit Bansal was reviewed and approved* by the following:

Michael F. Modest
Distinguished Professor of Mechanical Engineering
Thesis Advisor

Daniel C. Haworth
Professor of Mechanical Engineering

Karen A. Thole
Professor of Mechanical Engineering
Head of the Department of Mechanical and Nuclear Engineering

*Signatures are on file in the Graduate School.

Abstract

Radiative heat loads from nonequilibrium shock-layer are of great concern in the design of modern spacecrafts. Simulation of shock-layer radiation requires accurate modeling of spectral absorption and emission coefficients of high-temperature plasma, and solving the Radiative Transfer Equation (RTE) at thousands of wavelengths. Although the line-by-line solution of the RTE is very accurate, it is computationally very expensive to couple a line-by-line model with flow-solvers. This thesis discusses a full-spectrum *k*-distribution spectral model that allows efficient evaluation of radiative heat loads in a hot plasma dominated by radiation from the atomic species N and O. Application of the new spectral model to shock-layer plasma radiation is demonstrated by solving the radiation transfer equation along the Stardust stagnation-line flow-field. The full-spectrum *k*-distribution method is reasonably accurate compared to the line-by-line method. For more extreme gradients in species concentrations and temperature, *k*-distributions were found not to be correlated. Challenges posed by the extreme nonequilibrium gas conditions were overcome by sorting atomic lines into a number of nonoverlapping groups. The detailed methodology of the grouping scheme is presented.

Although the full-spectrum *k*-distribution approach make it possible to evaluate radiative fluxes at a fraction of the cost needed for line-by-line calculations, it is not very efficient to construct them from raw line-by-line absorption coefficient data. An accurate and compact narrow-band *k*-distribution database is developed for the lines of N and O. It was observed that the overlap between the two atomic species N and O is almost insignificant. This is a very important observation as it allowed databasing *k*-distributions from the two species independently. The database allows users to calculate desired full-spectrum *k*-distributions through look-up and interpolation. The accuracy of the database was tested by comparing narrow-band mean absorption coefficients and narrow-band emissivities with those obtained from line-by-line calculations. Application of the database in constructing full-spectrum *k*-distributions accurately and efficiently is discussed. Results from a number of heat transfer calculations and cpu-time studies are presented.

Table of Contents

List of Figures vi

List of Tables viii

List of Symbols ix

Chapter 1
Introduction 1
1.1 Background and Motivation . . . 1
1.2 Overview of Radiative Heat Transfer in Hypersonic Reentry Flows . . . 2
1.3 Importance of Ablation in Shock-layer Radiation . . . 4
1.4 Flow-Field–Radiation Coupling . . . 5
1.5 Hypersonic Radiative Property Models . . . 6
1.6 Radiative Transfer Equation . . . 7
1.7 RTE solution methods . . . 8
1.8 Spectral Modeling of the RTE . . . 10
1.9 The Reordering Concept and the *k*-distribution Model . . . 12

Chapter 2
Atomic Radiation 14
2.1 Structure of an Atom . . . 16
2.2 Bound-Bound Radiation . . . 17
2.3 Bound-Free and Free-Free Continuum Radiation . . . 19
2.4 Nonequilibrium and the Quasi Steady State Assumption . . . 20

Chapter 3
Correlated-*k* Distributions 24
3.1 Full-Spectrum *k*-Distribution Method . . . 24
3.2 Reference State . . . 26
3.3 Application of FSCK Method to Two-Cell Problem . . . 27
3.4 Stardust Reentry Problem . . . 27

Chapter 4
Multi-Group *k*-Distributions 31
4.1 Theoretical Formulation of Multi-Group *k*-Distribution Model . . . 35
4.2 Application of the Multi-Group *k*-Distribution Method to Heat Transfer Calculations . . . 36

Chapter 5
***k*-Distribution Database** **38**
5.1 Narrow-Band ***k***-Distribution for Mixture of Species 38
5.2 Database Generation 42
5.3 Databasing for Continuum Properties 44
5.4 Assembly of Full-Spectrum *k*-Distributions from Narrow-Band Database 45
5.5 Application of the Database 46
5.6 Sample Calculations 46
5.7 Computational Efficiency 47

Chapter 6
Conclusion and Future Work **53**
6.1 Conclusion 53
6.2 Future Work 54

Bibliography **60**

List of Figures

1.1 Picture of a spacecraft entering an atmosphere at hypersonic speed 2
1.2 A schematic description of the tangent-slab method 10

2.1 Stardust stagnation-line flow-field at peak heating (61.8 km altitude) 14
2.2 Emission energy along the stagnation-line of the Stardust vehicle 15
2.3 Sample absorption spectrum of N; $n_N = 5.0 \times 10^{16}$ cm^{-3}, $n_{N^+} = 5.0 \times 10^{14}$ cm^{-3}, $n_e = 5.0 \times 10^{15}$ cm^{-3}, T_e = 10000K, T= 15000K 15
2.4 Distribution of electrons in 2p orbital 16
2.5 Comparison of the QSS population with the Boltzmann population for N; $n_N = 5.0 \times 10^{16}$ cm^{-3}, $n_{N^+} = 5.0 \times 10^{14}$ cm^{-3}, $n_e = 5.0 \times 10^{15}$ cm^{-3}, T_e = 10000K, T= 15000K 22
2.6 Comparison of radiative heat flux for the Stardust stagnation line flow-field: Boltzmann vs. non-Boltzmann 22

3.1 Absorption Spectrum of N (left) and corresponding k-distribution (right); $n_N = 5.0 \times 10^{16}$ cm^{-3}, $n_{N^+} = 1.0 \times 10^{16}$ cm^{-3}, $n_e = 2.0 \times 10^{16}$ cm^{-3}, T_e = 10000K 26
3.2 A schematic of a two-cell problem 28
3.3 Comparison of k-distributions of N for conditions given in Table 3.1 29
3.4 Comparison of k-distributions of O for conditions given in Table 3.1 29
3.5 Comparison of heat flux along the stagnation line of the Stardust peak heating flow-field 30
3.6 Comparison of divergence of heat flux along the stagnation line of the Stardust peak heating flow-field 30

4.1 Dependence of absorption line strength of atomic N on electron temperature 32
4.2 Dependence of absorption line strength of atomic O on electron temperature 32
4.3 Spectral groups of atomic lines of N 33
4.4 Spectral groups of atomic lines of O 34
4.5 Heat flux along the Stardust stagnation-line flow-field for multi-group model 37
4.6 Divergence of heat flux along the Stardust stagnation-line flow-field for multi-group model 37

5.1 Sample narrow-band k-distributions for N and O; $n_e = 2.70 \times 10^{15}$ cm^{-3}, T_e = 10000K, T= 15000K 42
5.2 Narrow-band mean absorption coefficient of N; $n_e = 5.0 \times 10^{15}$ cm^{-3}, T_e = 10000K, T= 15000K 48
5.3 Narrow-band emissivity of N; $n_e = 5.0 \times 10^{15}$ cm^{-3}, T_e = 10000K, T= 15000K 48
5.4 Narrow-band mean absorption coefficient of O; $n_e = 5.0 \times 10^{15}$ cm^{-3}, T_e = 10000K, T= 15000K 49
5.5 Narrow-band emissivity of O; $n_e = 5.0 \times 10^{15}$ cm^{-3}, T_e = 10000K, T= 15000K 49

5.6 k-distribution assembly ; $n_N = 5.0 \times 10^{16}$ cm^{-3}, $n_{N^+} = 5.0 \times 10^{14}$ cm^{-3}, $n_O = 5.0 \times 10^{16}$ cm^{-3}, $n_{O^+} = 5.0 \times 10^{14}$ cm^{-3}, $n_e = 5.0 \times 10^{15}$ cm^{-3}, T$_e$ = 10000K, T= 15000K 50
5.7 Database results for heat flux along the stagnation-line of the Stardust peak heating flow-field 51
5.8 Database results for divergence of heat flux along the stagnation-line of the Stardust peak heating flow-field 51

List of Tables

3.1 Flow conditions for the two cells 28
3.2 Heat flux exiting the cold cell (W/cm^2) 28

4.1 Heat flux exiting the cold cell (W/cm^2) for multi-group model 36

5.1 Database results for Wall heat flux, (W/cm^2) 50
5.2 Computational time comparison (ms) 52

1 Details of electronic states of N 55
2 Details of electronic states of O 56
3 Narrow-band details 57
4 Datapoints for the narrow-band database 59

List of Symbols

c	speed of light, 2.9979×10^8 ms^{-1}
f	k-distribution, cm
$f^{'}$	normalized k-distribution, cm^{-2}
g	cumulative k-distribution
h	Planck's constant, 6.6262×10^{-34} Js
I	intensity, (W/cm^{2}sr)
k	absorption coefficient variable, cm^{-1}
$k^{'}$	absorption cross-section variable, cm^2
m	atomic mass, kg
M	Total number of narrow-bands
$\underline{n}$	number density (vector), cm^{-3}
T	temperature, K

GreekSymbols

κ	absorption coefficient, cm^{-1}
$\kappa^{'}$	absorption cross-section, cm^2
λ	wavelength, Å
$\underline{\phi}$	gas state vector
Φ	Line shape function

Subscripts

b	blackbody

bf bound-free

cl line center

D Doppler

e electron

ff free-free

k at a given value of reordered absorption coefficient

$k^{'}$ at a given value of reordered absorption cross-section

g at a given value of cumulative k-distribution

m for a given narrow-band

P Planck-mean

S Stark

U upper state

L lower state

λ at a given wavelength

Superscripts

bb bound-bound

q N (atomic nitrogen), or O (atomic oxygen)

$cont$ continuum radiation

Chapter 1

Introduction

1.1 Background and Motivation

The design of space vehicles is a task of very high complexities. While entering into the atmosphere of a planet or other planet-like bodies at hypersonic speeds, spacecrafts dissipate a large amount of their kinetic energy into heat through shock-waves. This phenomenon is known as aerocapture. A picture of a spacecraft entering into atmosphere at hypersonic speed is shown in Fig. 1.1. A spacecraft uses the atmospheric drag to reduce its speed while entering into the atmosphere. This is in contrast to the propulsive capture, where the vehicle is slowed down using a propulsion system. A large amount of the heat generated in the aerocapture process is absorbed by the thermal protection system (TPS), a heat absorbing blanket on the surface of the spacecraft. Hot ionized plasma occupies the region between the spacecraft and the shock-wave. A part from severe convective heat loads, radiation from the shock-layer may contribute a significant part toward the total heat load. However, for vehicles reentering from low earth orbits or ballistic missiles, the shock-layers are relatively cooler and effect of radiation is not significant. In general, the heat transfer rates increase with the vehicle radius of curvature and reentry velocity, making radiative heating very critical for larger space vehicles returning from deep-space missions at velocities as high as 13-14 km/s. The United States have successfully landed a number of manned missions on the lunar surface, and a number of unmanned probes on the surface of Mars. However, a number of challenges need to be overcome before crewed missions to nearby planetary bodies, including Mars, become possible. For Mars missions, robotic systems landed so far had mass below 0.6 metric tons [1]. However, future manned mission will require landing of significantly heavier systems (40-80 metric tons). This makes the design of the TPS critical, as it will have a direct impact on the overall weight of the system. The design of new generation space vehicles will require an optimum design of the TPS. Accurate computations of the radiative heat load are absolutely necessary for the design of the TPS, because uncertainties of the order of even 20% may have important system design implications.

Modelling shock-layer radiation is a very complicated and computationally expensive task. Even for earth reentry conditions from deep-space or lunar return missions, the shock-layer radiation phenomenon is not well understood. All earlier radiation studies relied on a number of simplifications. Most efforts,

so far, have been directed toward solving radiation independently from the flow solvers. However, the presence of a strong radiation field may significantly alter the population distribution of various radiating species, and a coupled radiative transport solution is desired for a more accurate solution. Also, most of the simulations done to date have been limited to simplified quasi-one-dimensional geometries (simple line-of-sight or tangent slab calculations) [2, 3]. Gas properties of high temperature air plasma, as found in the shock-layer of a spacecraft during atmospheric entry, have very erratic spectral behavior, varying by orders of magnitude over tiny spectral regions. The strong spectral structure of the radiative emission requires a line-by-line (LBL) solution of the Radiative Transfer Equation (RTE) at several hundred thousand wavelengths, making it prohibitively expensive. Therefore, most studies focused on approximate spectral models for performing radiation calculations. As a consequence of all these simplifications, the predicted radiative heat load onto the spacecraft may be very unreliable. The biggest hurdle in simulating radiation phenomenon exactly is the vast computational resources required by the line-by-line solution of the RTE. It is, therefore, absolutely necessary to develop a spectral radiation model that can predict radiative heat loads in hypersonic shock-layers accurately and, at the same time, efficiently. The radiation model must include sophisticated spectral modeling so that number of RTE evaluations can be reduced.

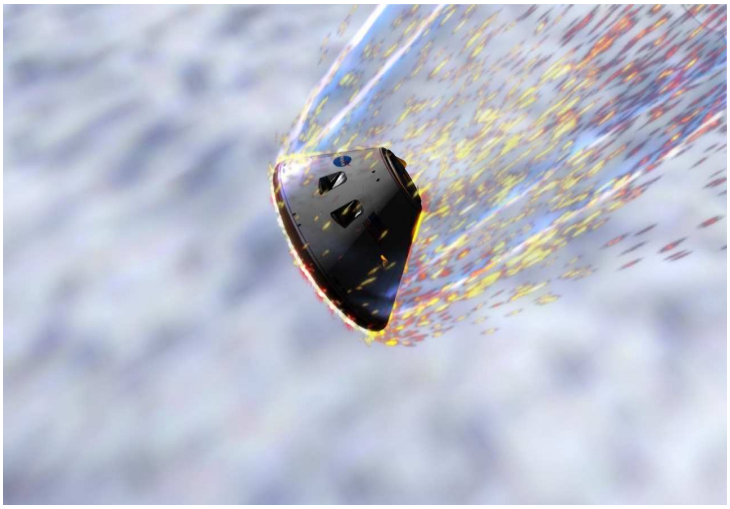

http ://www:nasa:gov/images/content/166931mainjsc2006e21479:jpg

Figure 1.1. Picture of a spacecraft entering an atmosphere at hypersonic speed

1.2 Overview of Radiative Heat Transfer in Hypersonic Reentry Flows

It has been recognized that space vehicles, while returning into the earth's atmosphere at hypersonic speeds, may be subjected to significant radiation loads from hot ionized plasma in the shock-layer, in addition to severe convective heat loads. A detailed survey of radiating shock-layers was presented by Anderson [4], identifying important and critical aspects of the aerothermal design of a spacecraft. Earlier investigations of shock-layer radiation were motivated by lunar return missions. During the Apollo

missions considerable resources were spent on quantification of the aerothermal environment around the reentry command module. These predictions were supported by a number of shock-tube experiments and two flight tests (Fire I and Fire II). The main purpose of these tests were to measure radiative heating rates and gather data for the development of theoretical models for the prediction of convective and radiative heat loads. The FIRE II data were later compared with theoretical models [2, 5]. It was established that gases in the shock-layer are highly dissociated, and the radiation field is dominated by the atomic species N and O.

Later researches explored the possibility of an aerocapture into the atmosphere of other planets like Venus [6], Mars [7, 8, 9], Jupiter [10, 11, 12], Neptune [13], and also Titan [14, 15], the biggest moon of Saturn. Of particular interest were Earth reentry for Mars return missions and aerocapture into the atmospheres of Titan and Mars.

Sutton [6] carried out an aerothermal analysis of Titan aerocapture for the Pioneer Venus mission. In contrast to the Earth's atmosphere of N_2/O_2, Venusian atmosphere is made up of 97 % CO_2 and 3% N_2 by volume. Radiation from CO_2/N_2 mixture is significant even at low temperatures, because of molecular band radiation from CN and CO. The radiative heating for Venus aerocapture was predicted to be nearly 10 times higher than for Earth. The atmosphere of Mars is very similar to that of Venus. A number of studies [8, 9] have predicted the extent of convective and radiative heating to Mars aerocapture vehicle under different entry conditions.

The Galileo probe entered into the (H_2-He) atmosphere of Jupiter on 7 December 1995. The entry velocities were as high as 40-50 km/s. For such severe entry conditions, a peak heating rate of 300 MW/m^2 was predicted [11]. The main radiating species in the Jovian aerocapture are H and H^+. Tiwari *et al.* [12] have estimated that the heat-shield weight for the Jovian entry system could be as much as 45% of the total weight of the probe. Thus, in such a scenario, there may be a significant effect of radiation on the shape change of the vehicle due to mass loss by ablation. This is in contrast to Mars and Venus aerocapture missions, where the levels of heating are not so severe as to significantly change the mass and shape of the probe. Among other earlier studies, a preliminary estimate of the convective–radiative heating environment for Neptune aerocapture in its H_2–He–CH_4 environment was carried out by Hollis *et al.* [13], indicating that the shock-layer radiation would contribute up to 80% of the total thermal load.

More recently, a number of radiation heat transfer studies have been made, primarily in the context of the Stardust [16, 17, 18, 19] and Titan aerocapture missions [15, 20]. The Stardust Sample return Capsule (SRC) was launched in February 1999 to retrieve interstellar dust samples. Stardust reentered Earth atmosphere in January 2006 at a velocity of 12.6 km/s, the fastest Earth reentry of an artificial vehicle to date. Extensive preflight coupled CFD–radiation simulations were carried out by Olynick *et al.* [16], emphasizing the need of accurate predictions of the radiative heat loads. The integrated radiative heat load for the Stardust vehicle is about 7% of the total. Park [18] found that most of the radiation gets absorbed in the boundary layer, and over half of the absorbed radiation is converted to convective heat flux, thereby increasing the convective heat flux by a factor of two. This is an important finding, which emphasises the significance of coupled radiation–flow analysis for the shock-layer.

A number of similar simulations have been performed for reentry into the atmosphere of Titan, Saturn's largest moon [15, 20, 21]. Titan has an atmosphere of N_2 with a small amount of methane. Methane

dissociates in the high-temperature flow to produce the cyanogen radical (CN), which is a very strong radiator. Analysis has predicted that radiative heating load from CN can be as high as 300 W/cm^2 at the stagnation point [15], more than seven times the convective fluxes. Radiative heating from the CN molecule was a major concern during the design of the European Space Agency's (ESA) Huygens probe. Huygens probe was released from the Cassini Saturn Orbiter on December 24, 2004; it entered the atmosphere of Titan on January 14, 2005. Peak radiative heat flux of 90 W/cm^2 was predicted for the Huygens probe, which is more than two times the convective heat flux [22, 23].

1.3 Importance of Ablation in Shock-layer Radiation

All spacecrafts are protected from severe heat loads by providing a protective heat-shield called TPS. Most heat-shields are made of carbon-phenolic or carbon-ceramic materials, which decay by means of pyrolysis, giving out large amount of gaseous products into the boundary layer. This process is known as ablation. The aerothermal environments for entry into various atmospheres were predicted to be very severe and produce massive ablation. The main products of TPS ablation are C_3, CO and other trace species; including C, HCN, CN and H [16]. In an arc-jet wind-tunnel experiment, the CN molecule was found to be the main radiating species in the shock layer over an ablating model [24]. The concentration of ablation products is generally higher in the cooler boundary layer region and, therefore, ablation species may have relatively larger absorption than emission. This may result in lowering of radiative heat fluxes, but, in turn, may also lead to larger convective fluxes due to a hotter boundary layer. The fourth positive band system of carbon monoxide, CO(4+), is one of the most important absorbing species among the ablation products. Scattering by solid carbon particles has also been attributed as a significant source of absorption of radiation in the boundary-layer. Early studies by Hoshizaki *et al.* [25] and Coleman [26] showed that absorption by carbonaceous species and other ablation species may lead to reduction in the radiative heat transfer by as much as factor of two.

For the Venus Pioneer mission, Sutton *et al.* [27] found that the attenuation of thermal radiation by ablation products might reduce the radiative heat to the body by 10 to 20 %. It was observed by Moss *et al.* [28, 29] that the flight data for the Pioneer-Venus and the Galileo missions showed higher heating rates than the predictions. Ablation was considered as one of the phenoemena leading to this disagreement. Sakai *et al.* [24] found that by including radiation from the spalled CN molecules and the blackbody radiation from spalled carbon-particles, the qualitative behavior of radiation can be reproduced by simulations.

Experimental studies of ablation phenomena have been made by many researchers. Raiche *et al.*[30] carried out a series of spectroscopic measurements in the arc-jet facility at NASA Ames Research Center. It was found through measurements that above the PICA(Phenolic Impregnated Carbon Ablators) ablator spalled ablation products lead to significant attenuation of radiation in the shock layer. They also found that emission from the ablation product is not significant. The main source of attenuation was attributed to the scattering by the solid carbon particles in the ablation products. They also observed some significant unstructured radiation from heated particles. This radiation was found to mimic the blackbody radiation at material surface temperature. Park [31] carried out a systematic analysis of the data acquired from the

arc-jet tests, using theoretical models of the particle properties.

1.4 Flow-Field–Radiation Coupling

Radiation energy can travel large distances into all directions. A large percentage of radiation energy emitted in the shock-layer is likely to escape from the region, resulting in cooling of the shock layer. This may change the flow parameters in the flow field, and, in turn, can affect radiative as well as convective heat loads. The consideration of cooling effects due to escape of radiation energy in flow field modelling is known as radiation–flow-field coupling. An estimate of the amount of coupling between radiation and the flow-field can be made by evaluating the radiative loss parameter Γ [32],

$$\Gamma = \frac{2q_{rad}}{\frac{1}{2}\rho_\infty V_\infty^3} \tag{1.1}$$

where q_{rad} is the radiative heat load, ρ_∞ is free stream density and V_∞ is free stream velocity, A Γ value greater than a few percent means that there is significant loss of energy from the shock-layer, and the flow is nonadiabatic and coupled to the radiation field. If a large amount of flow energy is converted to radiation, the shock-layer is cooled and there is significant impact on fluid dynamics and chemical kinetics of the flow. The effect of coupling is to reduce the total heat loads to the body of the spacecraft. For typical Titan aerocapture conditions Γ was found to exceed 40% near peak radiative heating, indicating that the flow is highly nonadiabatic. In contrast, Γ is only about 1% for the Fire-II flight experiment, and about 15% for Galileo [20]. Depending on the magnitude of coupling, radiation effects around a hypersonic plasma can be accounted for in two ways

1. Uncoupled- In this case the flow field is assumed to be adiabatic, and the effects of radiation on the flow field are not considered. As the shock layer gas may be considerably cooled due to radiation escape from the shocklayer, this may result in considerable overestimation of convective and radiative heat loads. However, the uncoupled approach is very simple and computationally very efficient. Tauber *et al.* [10] have provided an approximate relation to account for the radiative cooling effect. In this approximation, the coupled radiative heating rates can be approximated from uncoupled heating rates by using the follwing formula

$$\frac{q_{rad}^{coup}}{q_{rad}^{uncoup}} = \frac{1}{1 + \kappa\Gamma^{0.7}} \tag{1.2}$$

where κ is an empirical constant, whose value is given equal to three in [32]. Most of the earlier studies were based on an uncoupled approach or the approximate model of Tauber*et al.*. Even today, the uncoupled approach is used by many researchers to get an estimate of radiative fluxes onto the spacecraft.

2. Coupled - When the effect of radiation is not small, the radiation equations must be solved in conjunction with the flow solver to account for the effect of radiation cooling on the thermal and chemical properties of gases in the shock-layer. As a line-by-line model is very expensive for coupled studies, most of the studies have utilized approximate spectral models for doing coupled calculations. A simplification of the fully coupled approach, which is often used, is the loosely coupled approach. In this approach

radiation is not solved at every iteration of the flow, but radiative properties are updated only after a number of flow iterations. Between two radiation iterations, the radiation field in the flow is kept fixed.

For optically thin conditions, coupled studies can be very much simplified. The analysis for optically thin cases requires evaluation of emission at each point in the flow field. Any interaction of the radiation with the flowfield can be neglected, as has been done by Wright *et al.* [20], who showed that the coupled radiative heating rates were lower by a factor of two than the uncoupled case for the Titan aerocapture mission. They also observed a reduction of about 30% in the convective heating rates.

Efforts have also been directed to couple ablation with radiation and flow solvers, as they are known to influence each other. A number of coupled radiation and ablation studies have been performed for Earth entries [16, 17, 18, 33]. Olynick *et al.*[16] presented a comprehensive methodology for predicting flow with coupled radiation and ablation. An application to the Stardust flow field showed that the forebody heat transfer is significantly reduced due to coupling of radiation and ablation. For the Apollo 4 case, the ablation and radiation coupling was found to decrease the radiative heating by 15% and the convective heating by 85% [33]. Fully coupled solutions for Venus entry probes were performed by Sutton *et al.*[27], with both ablation and radiation. It was found that radiative heating toward the body is attenuated in the boundary layer for Venusian entries. This attenuation reduces the radiative heating to the body by 10 to 20 %.

1.5 Hypersonic Radiative Property Models

RAD/EQUIL, is one of the earliest and widely-used radiation codes developed by Nicolet [34]. The RAD/EQUIL code includes contributions from atomic continua, atomic lines and approximate models for molecules (bandless model based on curve-fit with temperature and wavelength as parameters). These radiation mechanism are discussed in detail in Chapter 2. For computational efficiency atomic lines spaced closely in the spectrum were combined into composite lines, and weak lines were not considered. Also, the RAD/EQUIL code calculates radiative properties by assuming thermodynamic equilibrium.

The Nonequilibrium Air Radiation (NEQAIR) model [35] was originally developed for the study of radiative properties of nonequilibrium, low density air plasmas. The NEQAIR96 model includes emission from the N, O, C, H, He, N_2^+, NO, CO, CN, O_2, C_2, OH and H_2 atomic and molecular systems. NEQAIR96 has been the most widely used code for performing nonequilibrium radiation calculations. This code models the spectral shape of each atomic line based on the atomic line data compiled by Wiese *et al.* [36]. Nearly four times as many lines are modelled in NEQAIR than in RAD/EQUIL. In NEQAIR, the molecular band systems are modeled using the line-by-line approach of Arnold *et al.*[37]. NEQAIR96 provides line-by-line data of nonequilibrium radiative properties of hypersonic shock layer plasmas, along with a primitive one-dimensional radiation transport algorithm. The nonequilibrium electronic state populations for various energy states are modelled based on the Quasi-Steady-State (QSS) assumption, which is also discussed in Chapter 2.

For typical nonequilibrium planetary reentry conditions, the RAD/EQUIL code was inadequate, because it assumed a Boltzmann distribution of the electronic states, which is incorrect in regions of nonequilibrium, and also because multi-band models are used to model molecular radiation. A recent

comparison by Hollis *et al.* [23] showed that RAD/EQUIL results for CN radiation for the Huygens mission differ by as much as 40% to 60% from those predicted by the NEQAIR code. In response to this, a number of revisions to the RAD/EQUIL code were introduced. Gally *et al.* [38, 39] developed two approximate correction methods to account for the non-Boltzmann population of atomic electronic states. A recent study by Johnston [40] showed that the curve-fit models of molecular bands in RAD/EQUIL overpredicts the radiative heat fluxes for CN.

NEQAIR is a line-by-line code, and, therefore, computationally very expensive. To reduce the computational cost of NEQAIR, the Langley Optimized Radiative Nonequilibrium (LORAN) code was developed [41]. The LORAN model uses the same QSS assumption to determine the electronic state population and utilizes the same Voigt line shape. The LORAN code uses nonuniform spectral resolution to resolve atom lines and atomic continua, thereby, requiring lesser spectral points compared to a uniformly spaced spectrum. In addition, radiation properties for the molecular band systems are calculated using a "smeared band" approximation instead of the line-by-line approach used in NEQAIR. The LORAN code uses band models, in which a number of spectral lines are grouped together to form composite lines. Grouping of lines in bands helps in speeding up the RTE evaluation. Hartung *et al.* [41] used the LORAN code to model the Fire II spectra and to examine lunar and Mars return conditions. The absorption and emission coefficients generated by the LORAN code have been shown to be comparable to those generated by the NEQAIR [42]. However, coupling the LORAN code with a flow solver is still computationally very expensive. Further efficiency improvements in the LORAN code lead to the development of the NOVAR algorithm. In NOVAR, the QSS distribution is replaced by a Boltzmann distribution. Also, for better efficiency, the implementation of the algorithm in the codes is quite different from the LORAN code.

A new High-temperature Aerothermodynamic Radiation model (HARA) developed by Johnston [40] utilizes comprehensive and updated atomic line data, accurate Stark broadening parameters, detailed atomic photoionization and negative ion photodetachment cross-sections. In the HARA code a very comprehensive Collision–radiative model is implemented for air species to determine nonequilibrium population of electronic states. Johnston's model has been validated by experimental data at a number of flight conditions. The HARA code applies the smeared-rotational band (SRB) model to model molecular radiation. Also, a tangent-slab radiative transport algorithm is applied for solving the radiative transfer equation.

More recently, Sohn *et al.* [43] have developed an efficient databasing scheme that has resulted in a significant reduction of computation time for spectral coefficients vis-a-vis NEQAIR. This database is based on NEQAIR, and includes all the features of the NEQAIR. Sohn *et al.* have demonstrated that their databasing scheme can be applied efficiently to generate accurate spectral coefficients for a given flow condition. In this work, this database scheme will be used as a base model to generate nonequilibrium spectral absorption and emission coefficients for different species.

1.6 Radiative Transfer Equation

The behavior of radiative heat transfer in an absorbing, emitting, and/or scattering medium is affected by a number of phenomena. Radiation travelling through a participating medium may be attenuated by

absorption and scattering. If scattering is ignored, the amount of radiation absorbed can be written as

$$(dI_\lambda)_{abs} = -\kappa_\lambda I_\lambda ds \tag{1.3}$$

where κ_λ is the linear absorption coefficient of the medium, I_λ is the intensity of incident radiation and ds is the distance travelled in space. Similarly, radiation can be augmented by emission. For the case of thermodynamic equilibrium the emission can be written as

$$(dI_\lambda)_{abs} = -\kappa_\lambda I_{b\lambda} ds \tag{1.4}$$

where $I_{b\lambda}$ is the Planck function. Combining Eqs.(1.3) and (1.4) gives the complete radiative transfer equation for a participating medium. The radiative transfer equation describes radiation intensity field in space as a function of location, direction of transfer and spectral variable λ.

$$\frac{dI_\lambda}{ds} = \kappa_\lambda (I_{b\lambda} - I_\lambda) \tag{1.5}$$

It has been found that neglecting scattering may not be valid for many practical flow conditions. Scattering by particulate matter (carbon primarily) can be important for some cases [34]. However, the scattering phenomena is not well enough understood to date to be described quantitatively. Consequently, most models neglect the interaction between the radiation field and any particulate matter. A preliminary theoretical model of the behavior of solid particles ejected into the shock-layer from an ablating heatshield is given in Ref. [31].

1.7 RTE solution methods

Solving a radiation problem is a two-step process: i.) Evaluation of gas properties for all gas conditions in the flow field, ii.) solution of the the Radiative Transfer Equation (RTE). The radiative transfer equation is a five-dimensional (3 space coordinates and 2 directions) integro-differential equation and is, consequently, very expensive to solve. A complete three-dimensional simulation with detailed spectral modelling is prohibitively expensive. Most simulations to date either employ a simple one-dimensional geometry with detailed line-by-line spectral models or full-geometry simulations with approximate spectral treatment; of course, the choice depends on the type of the problem. Exact solutions of the RTE for complicated three-dimensional geometries are not possible. Most simulations done to date have been limited to simplified quasi-one-dimensional geometries (simple line-of-sight or tangent slab calculations). However, the use of the tangent-slab approximation may yield conservative estimates of heat fluxes, because it considers a layer of infinite width and neglects the curvature effects of the body of the spacecraft [20]. For more general geometries and flow conditions a number of approximate methods have been developed, such as discrete ordinate method, spherical harmonics method, and the statistical Monte Carlo method.

For optically thin situations Bose *et al.* [44] have presented a three-dimensional transport model based on geometric view factors between the emitting volume and surface elements of the spacecraft. In this

method, the emitted energy in each cell is calculated from an uncoupled flow field solution, using the line-by-line or some approximate spectral model. The emitted energy is assumed to propagate isotropically in all directions without any absorption. The amount of energy hitting at a particular surface element from a particular cell is evaluated based on view-factors between the two elements. Then, the total radiative flux is evaluated by summing up contributions from all cells. This method is a significant improvement over the tangent slab method for optically thin situations. However, in reality, the intensity field is not isotropic, and there will be absorption inside the shock-layer. A ray tracing technique, that accounts for the absorption of radiation, was presented by Osawa *et al.* [3]. For efficient evaluation of heat fluxes, they optimized the angular integration scheme using a set of Gauss quadrature points for integrating intensity over the solid angle. A 25% reduction in heatflux at the stagnation point was reported compared to the tangent slab method for the Huygens probe.

Hartung *et al.* [45] employed the modified differential approximation (MDA) method of Modest [46] to solve the RTE in a three-dimensional flow-field. In MDA method the complicated integro-differential equation of radiative transport is transformed into a set of partial differential equations, which are relatively simple to solve. A difference of 10% was reported in the wall radiative heat loads compared to the tangent-slab method. Surzhikov *et al.* [47] applied the P1-approximation of the Spherical Harmonics method (SHM) to calculate radiation heat transfer for FIRE II vehicle; however, for the same problem they also calculated the radiative fluxes by a ray-tracing method (RTM).

In contrast to these higher-order approximate methods, the statistical Monte-Carlo method, while computationally expensive, can be applied to radiation problems of any complexity (strong spectral, spatial or directional variation of radiative properties, etc.). A three-dimensional Photon Monte Carlo (PMC) method was developed by Wang *et al.* [48] to solve radiation problem in strongly nongray thick media. The PMC model is not very cost effective to apply to simple geometries. However, the PMC method is a powerful tool for radiation analysis in complex geometries and flow conditions. The PMC method simulates radiation by tracing photon bundles from an emission location to a termination location. The locations of emitting photon bundles at each cell are determined using random number relations. Each cell emits a number of rays proportional to the ratio of the cell's emission energy to total emission energy. This method has been applied to perform tightly-coupled calculation for the Stardust Vehicle [49, 50, 51].

As this work focuses on the spectral modeling of radiative properties, it is applicable to any RTE solver. To keep the analysis simple, only the tangent slab RTE solution method has been considered in this work. A complete description of this method is given below.

Tangent slab Method

When the shock-layer thickness is much smaller than the radius of the body, the thin shock layer region can be approximated by a one-dimensional gas slab. The tangent slab method is the simplest radiation solution method. It considers a one-dimensional plane-parallel medium (a one-dimensional slab with properties varying only in the transverse direction) at radiative equilibrium (i.e., radiation is the only mode of heat transfer) or a known temperature field. The method is valid for a gray medium or on a spectral basis for a nongray medium. For shocklayer radiation calculations, temperature field is generally known from CFD simulations. Thus, for this very simple case Eq. (1.5) can be solved for the spectral

intensity I_λ as [52].

$$I_\lambda(\tau, \underline{s}) = I_{w\lambda}(\underline{s})e^{-\tau_s} + \int_0^{\tau_s} I_{b\lambda}(\underline{\phi}, \underline{s})e^{-(\tau_s - \tau_{s'})}d\tau_{s'} \tag{1.6}$$

where $\tau_s = \int_0^s \kappa_\lambda(\underline{s})ds$ is the optical thickness measured in the $\underline{s}$ direction. In Eq.(1.6) the first term denotes attenuation of wall intensity after traveling an optical distance τ_s, while the second term denotes the augmentation of intensity by emission, which itself gets attenuated through a distance $\tau_s - \tau_{s'}$. In general, intensity is a function of polar angle θ and azimuthal angle ψ, as shown in Fig 1.2. It is assumed that the radiative properties are uniform in all azimuthal directions, i.e., they do not depend on ψ. Equation (1.6) is simplified by substituting $\tau_s = \tau/\cos\theta$ and $\tau_{s'} = \tau'/\cos\theta$. The heat flux at any point within the medium can be obtained from the intensity and is given as

$$q(\tau) = 2J_1E_3(\tau) - 2J_2E_3(\tau_L - \tau) + 2\pi\int_0^\tau I_bE_2(\tau - \tau')d\tau' - 2\pi\int_\tau^{\tau_L} I_bE_2(\tau' - \tau)d\tau' \tag{1.7}$$

where E_2 and E_3 are exponential integrals of order two and three, respectively. J_1 and J_2 are wall radiosities, which will be zero for cold black wall conditions.

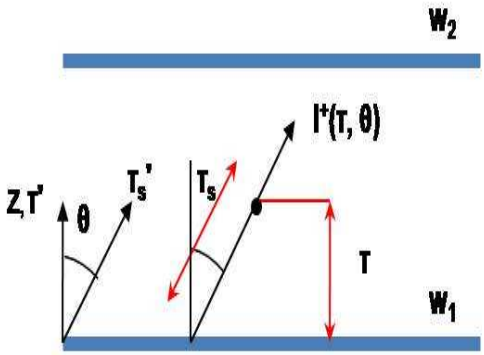

Figure 1.2. A schematic description of the tangent-slab method

1.8 Spectral Modeling of the RTE

The very earliest shock-layer radiation simulations employed transparent and gray-gas assumptions [53]. This means that radiation properties of the medium are independent of wavelength and all emitted energy leaves the system without being absorbed. The effect of radiation absorption was first studied by Howe and Viegas [54], who modelled a gray absorption coefficient, including the effects of self absorption and absorption in the cooler boundary layer. However, results of Hoshikawa *et al.* [55] showed that the gray approximation is not better than neglecting absorption. This is true, because molecular radiation is optically thin and there are very few atomic lines, which have strong self absorption. Olstad [56] first indicated that non-gray self-absorption may have a significant effect by substantially reducing radiative heat transfer. Hoshikawa *et al.* [55] proved that non-gray self-absorption is indeed very important. The significance of atomic lines was first shown by Biberman *et al.*[57]. Earlier spectral models for atoms

were simply based on step-models [56] and molecular band radiation was usually modelled using multi-band models based on curve-fit methods [34]. All these models were significantly less inaccurate than more detailed line-by-line models.

With the advent of powerful computers, line-by-line calculations have become possible, though very expensive. Line-by-line calculations require very accurate absorption coefficient data at hundreds of thousands of wavelengths. Because of strong opacity of atomic lines and the erratic nature of molecular band-spectra, very fine spectral resolution is required to represent the absorption and emission coefficients with desired accuracy. The RTE must be solved at each wavelength, and the total intensity is calculated by applying a suitable integration scheme in wavelength space.

Since each molecular-band consists of a large number of rotational lines, the solution of the RTE is much more expensive for molecules than for atomic lines or continuum. Many approximate and efficient spectral models have been developed for molecular bands, particularly for infrared applications in atmospheric and combustion studies. In all these models, the spectrum is divided into a number of bands, and the properties over a given band are assumed uniform. The RTE is solved independently for each band and the total heat transfer is found by summing the results over all the bands.

For optically thin shock-layer radiation, a smeared rotational band (SRB) model was developed by Patch *et al.* [58], which was recently extended by Chambers [59] to higher-order accuracy and multi-temperature conditions. This method is used in the LORAN and the HARA codes to model molecular radiation. For typical earth reentry conditions there is very little emission from the molecules. Even when there is significant emission from molecules, the field is optically thin, and the SRB model can provide very accurate results. However, it was found that even gray calculations would be excellent for optically thin situations found in typical reentry conditions. In the SRB model a number of rotational lines are combined such that the average shape of each vibrational band is captured. Also, the formulation is done in such a way that the method returns an accurate total radiative flux in the optically thin limit.

It was shown that for partially optically-thick conditions the conventional smeared-rotational band approach is inadequate ; e.g., representing the CN violet band by SRB model leads to over-prediction of the radiative flux by up to 40% relative to the LBL method [60]. Johnston *et al.* [60] proposed a simple modification to the SRB model that improves its accuracy in partially optically-thick conditions. In the new model, called SRBC (smeared-rotational band corrected), the rotational temperature is tuned in such a way that the band shape conforms well with the actual shape and gives more accurate results than the conventional SRB model. Johnston *et al.* reported that their results using the SRBC model agree to within 5% of the line-by-line results.

A new scheme named Planck–Rosseland–gray (PRG) model was developed by Sakai *et al.* [61] to reduce the computing time for radiative transport calculations. It is well known that the Planck approximation and the Rosseland or diffusion approximations are good for optically thin and thick situations, respectively. An actual flow field is neither optically thick nor optically thin over the entire spectrum. In this model the absorption coefficient at a given wavelength point at a flow condition is classified into one of the Planck, Rosseland, or gray-gas groups, where gray group refers to optically intermediate conditions. The radiative heat fluxes are computed for each group,and the true value of the radiative heat flux is given by the sum of radiative heat flux values for each of these three groups. However, grouping

of wavelength in each of the group is not straightforward. Sakai *et al.* applied an iterative scheme to implement this grouping model. It was reported that this model reduces the computing time of radiative transport by a factor of 10 compared to a multi-band method. An application of this method by Sakai *et al.* [24] to various planetary entry conditions showed that the PRG model can produce very accurate results compared to the line-by-line or multi-band models.

1.9 The Reordering Concept and the *k*-distribution Model

The idea behind the reordering method is to replace the spectral integration over wavelengths with integration over the absorption coefficient. Hermann and Schade [62] introduced the reordering concept for high-temperature atomic radiation in the case of cylindrical nitrogen arcs. This model is very similar to the narrow-band based correlated-*k* model, which is the main theme of this work.

The absorption coefficient κ_λ oscillates rapidly across the spectrum, attaining the same value many times (at different wavelengths). It has been shown that, for a small spectral interval (narrow-band) in a homogeneous medium, the absorption coefficients can be reordered into a monotonic *k*-distribution, which yields exact results at a fraction of the computational cost required by line-by-line methods [63, 64]. Early *k*-distributions were developed in the field of meteorology. In the heat transfer area important work on *k*-distributions was carried out by Rivière *et al.* [65, 66, 67]. More recently, such *k*-distribution methods have been applied to the full spectrum and to inhomogeneous media [68, 69].

The full-spectrum scheme was first implemented in the Weighted Sum of Gray Gases (WSGG) model. The concept of the WSGG approach was first presented by Hottel and Sarofim[70] for applications to the zonal method. Modest [71] generalized the WSGG model for use with any arbitrary solution method, although he assumed that the absorption coefficients and weights are spatially independent. In this method the nongray gas is replaced by a number of gray gases, for which the heat transfer rates are calculated independently by solving the RTE with weighted emissive powers for each of the gray gases. The total heat flux is then found by adding the fluxes of all gray gases.

In the WSGG model, the average absorption coefficients and weight factor for each gray-gas are found from total emissivity (or transmissivity) data. Denison and Webb [72, 73] developed the Spectral Line Based WSGG (SLW) model based on detailed spectral line data. In this model, the absorption coefficient is used as the basic radiative property rather than transmissivity or band absorptance. Denison and Webb also extended the SLW model to nonisothermal and nonhomogeneous media. For high temperature applications Rivière *et al.*[74] developed the Absorption Distribution Function (ADF) approach, which is almost identical to the SLW model with only the difference being the evaluation of the gray-gas weights. This method was further generalized by introducing fictitious gases (ADFFG), employing a joint distribution function that separates the gas into two or more fictitious gases, and is designed to be more suitable for the treatment of nonhomogeneous media [75]. It was later demonstrated by Zhang and Modest that the WSGG/SLW/ADG models are step approximations to the smoother full-spectrum *k*-distribution model [68].

While the *k*-distribution method is exact for a homogeneous medium, significant errors may occur when applied to strongly inhomogeneous media. Over the years a number of new adaptations of the

k-distribution method have evolved. The problem of inhomogeneity is addressed by using one of two different approaches: the scaling approximation or the assumption of a correlated *k*-distribution [69]. Both the scaled and correlated-*k* approaches may result in significant errors when dealing with inhomogeneous media, because neither the scaled nor the the correlated assumptions are ever truly accurate. The resulting errors and the applicability of the scaled and correlated-*k* methods have been discussed by Modest [69]. It was recognized [65, 66, 67] that, in high temperature combustion applications, with significant temperature changes totally different spectral lines dominate the radiative transfer, and the assumption of a correlated absorption coefficient breaks down. Similarly, in a mixture of gases the correlation breaks down in the presence of strong concentration gradients, as recognized by Modest and Zhang [68].

To overcome some of these difficulties, Modest and Zhang developed the multi-scale full-spectrum correlated-*k* distribution method MSFSCK [76, 77, 78] (similar to the fictitious gas model of [75]), where different lines are placed into separate "scales" based on their temperature dependence, and the multi-group full-spectrum correlated-*k* distribution method MGFSCK [79, 80], where different spectral positions are placed into different spectral groups according to their temperature and pressure dependence. The concept behind these two approaches is to break up the gas absorption coefficients into pieces that are as correlated or scaled as possible. The multi-group model has the advantage that it avoids the problem of overlap between the spectral groups. In contrast, in the MSFSCK method the approximate treatment of overlap between different scales may lead to additional inaccuracy. Mixing of scale is addressed by introducing an overlap parameter to approximate the effect of overlap among scales. The multi-group FSK method has been shown to achieve great accuracy for a single gas species with inhomogeneity in temperature whereas the multi-scale MSFSK method can efficiently treat mixtures of absorbing gases with severe species inhomogeneity. However, challenges still remain for radiative calculations in a gas mixture containing both temperature and species concentration inhomogeneities. A new hybrid multi-scale multi-group FSK MSMGFSK method was developed [81, 82]. This method resolves the absorption coefficient of an individual species in a mixture as one of its scales. Within each scale, the wavenumbers are placed into into exclusive correlated groups.

The use of the correlated-*k* method for solving high-temperature shock-generated radiation problems appears very attractive; however, applying it to hypersonic plasmas introduces a number of new difficulties due to thermodynamic nonequilibrium and the presence of a significant number of radiating species. The shock-layer of a reentry space vehicle is marked by the presence of extreme temperature and concentration gradients. The nonequilibrium flow field cannot be represented by a single temperature, and the radiation field is governed by a number of collisional processes. Finally, monatomic species have relatively few spectral lines, but of extreme opacity, making the behavior of line wings of overriding importance. These phenomena make the shock radiation problem very challenging from an FSCK point of view.

Chapter 2

Atomic Radiation

In high-temperature nonequilibrium flows the diatomic species may become highly dissociated and emission from the resulting two atomic species N and O, including bound-bound, bound-free and free-free transitions, is the major source of radiation from the shock layer in earth atmosphere entry conditions [83]. This can be verified by considering the peak heating stagnation line flow-field of the Stardust vehicle shown in Fig. 2.1. A comparison of the emission energy between atoms (N and O) and molecules (N_2, N_2^+, NO, O_2) is given in Fig. 2.2. It is clear that emission from atomic species is orders of magnitude higher than that of all the molecules species added together. For atomic radiation, atomic bound-bound lines contribute more to total radiation than the bound-free and free-free transitions. A typical absorption spectrum of atomic N is shown in Fig 2.3, showing distinct peaks along with the relatively constant continuum radiation. There are three basic mechanisms that lead to emission or absorption of a photon: spontaneous emission, stimulated emission and stimulated absorption, all leading to excitation/de-excitation of atoms from one energy state to another. In the case of continuum radiation, the excited state is a free state.

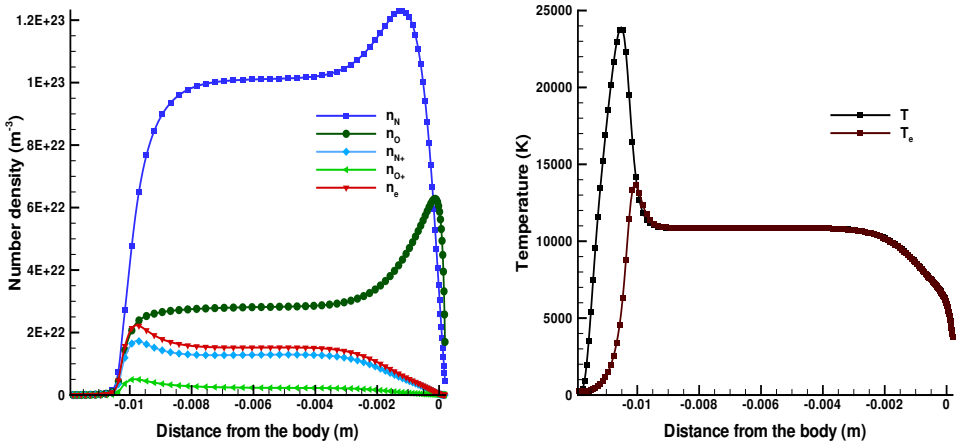

Figure 2.1. Stardust stagnation-line flow-field at peak heating (61.8 km altitude)

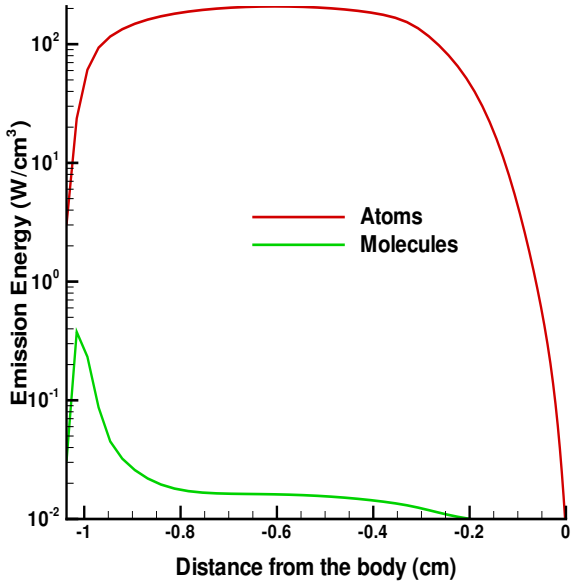

Figure 2.2. Emission energy along the stagnation-line of the Stardust vehicle

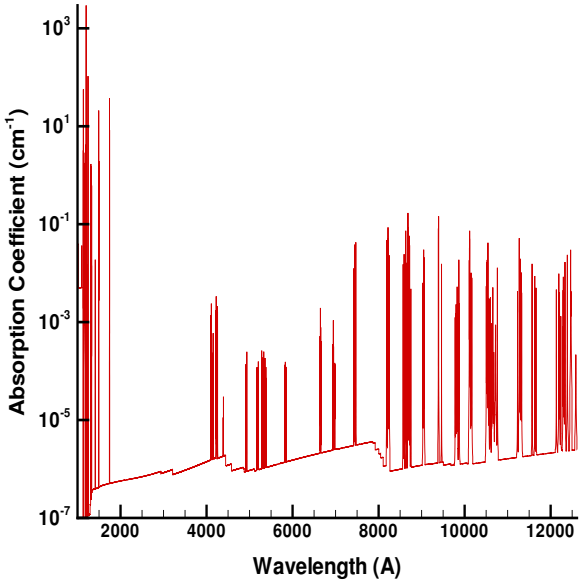

Figure 2.3. Sample absorption spectrum of N; $n_N = 5.0 \times 10^{16}$ cm^{-3}, $n_{N^+} = 5.0 \times 10^{14}$ cm^{-3}, $n_e = 5.0 \times 10^{15}$ cm^{-3}, T_e = 10000K, T= 15000K

2.1 Structure of an Atom

All atoms have a number of distinct energy levels, called electronic states. An electronic state of an atom is described by a set quantum number, represented by the following term symbol

$$nl^{x(2S+1)}L_J \tag{2.1}$$

where the various symbols represents the following
$n \Rightarrow$ principal quantum number,
$l \Rightarrow$ azimuthal quantum number of active orbital,
$x \Rightarrow$ number of equivalent active electrons,
$S \Rightarrow$ total spin of the electrons,
$L \Rightarrow$ total azimuthal quantum number ($L = 0 \rightarrow S$, $L = 1 \rightarrow P$, $L = 2 \rightarrow D$),
$J \Rightarrow$ total angular momentum quantum number ($\underline{L} + \underline{S}$)

As an example, we can consider the ground state of atomic N, which has 7 electrons with the following electron configuration $1s^2 2s^2 2p^3$. The distribution of electrons in the active $2p$ orbital for this state is given in Fig. 2.4

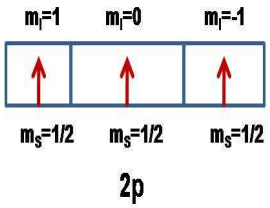

Figure 2.4. Distribution of electrons in 2p orbital

The value of L is equal to the sum of magnetic quantum numbers m_l and value of S is equal to the sum of spin quantum number m_s. For the above electron configuration, the term symbol can be written as $2p^3\ {}^4S_{3/2}$. In another example, one can consider an excited state of atomic N, with the following electron configuration $1s^2 2s^2 2p^2 3s^1$. The distribution of electrons in $3s$ orbital and the term symbol for the energy levels are given as

$$3s^1\ {}^4P_{1/2},\quad 3s^1\ {}^4P_{3/2},\quad 3s^1\ {}^4P_{5/2} \tag{2.2}$$

Note that there are three different states for the same electronic configuration. This happens due to spin-orbit coupling, also known as R-S coupling. Each of the terms here represents an energy level. The details of various electronic states of N and O, as used in NEQAIR and in the database developed by Sohn *at al.* [43], are given in Table 1 and 2, respectively [84]. The table lists the term-symbol, energy value and degeneracy for each of the energy states. The higher electronic states in this table are composite states formed by combining a number of different electronic states. There are a total of 22 energy levels for N and 19 levels for O. Quantum mechanics predict a number of transitions from one electronic state to the

other, leading to emission or absorption of a photon at a specific wavelength. Some electronic transitions are more probable than others and, therefore, some lines are stronger than others. NEQAIR and the database of Sohn *et al.* list 170 lines for N and 86 lines for O [35, 43]. Recently, the data set for atomic radiation has been expanded to include more lines of nitrogen and oxygen, as given in the NIST-15 and Opacity Project-16 database. In the modified dataset, the number of lines is 914 for N and 682 for O. Park [5] included the extended atomic line data in the NEQAIR code to perform radiation calculations for Fire II and Apollo 4 vehicles. He concluded that inclusion of new atomic lines significantly increased the radiative intensity. An update of the NEQAIR code was presented by McCorkle *et al.* [85] using the extended atomic line data and updated Stark broadening database. Similar updated atomic and molecular data have been compiled by Chauveau *et al.* [86, 87] and Johnston [40] .

As the modified dataset has not yet been implemented in the work of Sohn *et al.*, the older version of the dataset will be used in this work.

2.2 Bound-Bound Radiation

Atomic lines result from transitions from one electronic state to the other. An excited electron may spontaneously move to a lower energy state by emitting a photon of appropriate wavelength. The spontaneous spectral emission coefficient is defined as

$$\varepsilon_\lambda(\underline{\phi}) = g_U n_U(\underline{\phi}) A_{UL} hc \Phi(T, T_e, n_e) \frac{1}{\lambda} \frac{1}{4\pi} \tag{2.3}$$

where $\phi = (T, T_e, \underline{n})$ is the gas state vector, $\underline{n}$ is the number density vector specifying concentrations of (neutral, ion and electron), and $\Phi(T, T_e, n_e)$ is the line shape function. T and T_e represent translational and free electron temperature, respectively. Stimulated emission and absorption, unlike spontaneous emission, are caused by the presence of photons in the vicinity of emitting or absorbing species. Combining stimulated emission and absorption coefficients, the effective volumetric absorption coefficient is given as

$$\kappa_\lambda(\underline{\phi}) = \Big(g_L n_L(\underline{\phi}) B_{LU} - g_U n_U(\underline{\phi}) B_{UL} \Big) \Phi(T, T_e, n_e) \frac{h}{\lambda} \tag{2.4}$$

Using the law of detailed balance, $g_L B_{LU} = g_U B_{UL}$, the absorption coefficient expression can be reduced to

$$\kappa_\lambda(\underline{\phi}) = \Big(n_L(\underline{\phi}) - n_U(\underline{\phi}) \Big) g_U B_{UL} \Phi(T, T_e, n_e) \frac{h}{\lambda} \tag{2.5}$$

Simplifying Eqs.(2.3) and (2.5), the absorption and emission coefficients from a single atomic line can be written as

$$\varepsilon_\lambda(\underline{\phi}) = \varepsilon^c_\lambda n_U(\underline{\phi}) \Phi(T, T_e, n_e) \tag{2.6}$$

$$\kappa_\lambda(\underline{\phi}) = \kappa^c_\lambda [n_L(\underline{\phi}) - n_U(\underline{\phi})] \Phi(T, T_e, n_e) = \kappa^c_\lambda \Delta n(\underline{\phi}) \Phi(T, T_e, n_e), \tag{2.7}$$

where κ_λ^c and ε_λ^c are constants, independent of gas conditions. The Einstein coefficients A_{UL} and B_{LU} are related according to the following relation

$$B_{UL} = \frac{\lambda^5}{8\pi hc} A_{UL} \tag{2.8}$$

Thus, the emission coefficient can be rewritten as

$$\varepsilon_\lambda(\underline{\phi}) = \kappa_\lambda(\underline{\phi}) \frac{2hc^2}{\lambda^5} \frac{n_U(\underline{\phi})}{n_L(\underline{\phi}) - n_U(\underline{\phi})} \Phi(T, T_e, n_e) = \kappa_\lambda(\underline{\phi}) I_{b\lambda}^{ne}(\phi) \Phi(T, T_e, n_e), \tag{2.9}$$

where $I_{b\lambda}^{ne}(\phi)$ is the nonequilibrium Planck function. At nonequilibrium the population ratio of upper to lower electronic states, n_L/n_U, replaces the exponential term in the Planck function [35], i.e.,

$$I_{b\lambda}(\phi) = \frac{2hc^2}{\lambda^5[e^{C_2/\lambda T} - 1]} = \frac{2hc^2}{\lambda^5} \frac{n_U(\underline{\phi})}{n_L(\underline{\phi}) - n_U(\underline{\phi})} \tag{2.10}$$

where C_2 is the second radiation constant. The absorption coefficient given by Eq. (2.7) may be negative in some nonequilibrium plasma conditions [88, 42]. Negative values occur when the stimulated emission exceeds stimulated absorption. This means that the population of upper energy level of an electronic transition is more than the population of lower energy level. Such a population inversion can occur when the higher energy levels, populated according to the temperature and chemistry of the hot shock-layer, are not able to relax in the colder boundary-layer. Negative values of absorption coefficient generally occur at larger wavelengths of the spectrum.

Most atomic lines are optically very thick and have strong self-absorption characteristics. More than 90% of the emission from these lines tends to be absorbed by the line itself over distances as short as 1mm. Thus, atomic line wings, rather than the line centers, are most important from a heat transfer point of view. Consequently, it is very important to represent the line shape accurately. The line shape can most realistically be described by the Voigt profile [35, 52]. The Voigt profile is defined by Lorentzian and Gaussian line half-widths at half-height. The line width is an important parameter as it specifies how far from the line center a line retains its strength before its contribution becomes insignificant. Usually, with a Voigt line profile a strong atomic line may remain important up to 25 to 50 line half-widths on each side of the line, since it is optical thicknesses of order unity that contribute most to the radiative transfer. The Lorentzian width depends on a number of broadening mechanisms. For the case of high-temperature plamas having high electron number densities, the Lorentz width is essentially governed by Stark broadening, while the Gaussian width comes from Doppler broadening. Bose *et al.* [83] studied the effects of various line broadening mechanisms on atomic radiation. They concluded that the Stark effect is the most important broadening mechanism. The Stark width b_S and Doppler width b_D can be written as [59]

$$b_S = 2b_{S,ref} \left(\frac{T_e}{T_{ref}} \right)^{0.33} \frac{N_e}{N_{e,ref}} \tag{2.11}$$

$$b_D = \lambda_{cl}\sqrt{\frac{2kT\ln 2}{mc^2}} \tag{2.12}$$

where $b_{S,ref}$ is a reference Stark width value at a reference electron temperature of $T_{ref} = 10,000$K, and reference electron density $N_{e,ref} = 10^{16}\text{cm}^{-3}$; λ_{cl} is the wavelength at the center of an atomic line and m is the mass of the radiating atom. The Voigt line shape function can be approximated as [35]

$$\begin{aligned}\Phi_\lambda = \Bigg[&(1-\frac{b_S}{b_V})e^{-2.772(\Delta\lambda/b_V)^2} + \frac{b_S}{b_V}/1 + 4(\Delta\lambda/b_V)^2 + \\ &0.016\frac{b_S}{b_V}(1-\frac{b_S}{b_V})(e^{-0.4(\Delta\lambda/b_V)^{2.25}} - \frac{10}{10+(\Delta\lambda/b_V)^{2.25}})\Bigg] \\ &\Bigg/\Bigg[b_S(1.065 + 0.447\frac{b_S}{b_V} + 0.058(\frac{b_S}{b_V})^2)\Bigg]\end{aligned} \tag{2.13}$$

$$b_V = 0.18121(1-sd^2) - (0.02365e^{0.6sd+0.00418e^{-1.9sd}}\sin(\pi sd)(b_d + b_S) \tag{2.14}$$

where

$$sd = \frac{b_S - b_d}{b_S + b_d} \tag{2.15}$$

2.3 Bound-Free and Free-Free Continuum Radiation

In addition to bound-bound transitions, there are two other mechanisms that lead to a change of energy levels by emission or absorption. These are transitions between a bound state to a dissociated state, leading to bound-free/free-bound radiation, and transitions between two free states, leading to free-free radiation [35, 43]. The free state is in the ionized state. In the bound-free case, the wavelength of transition is determined by the kinetic energy of the free electron E_k, as

$$\lambda = \frac{hc}{\Delta E} = \frac{hc}{E_\infty - E_i + E_k} \tag{2.16}$$

where E_∞ is the ionization potential of the atom and E_i is the energy of the i-th bound-level. Since the electron energy is continuously distributed according to a Maxwellian distribution, the radiation is essentially continuous, unlike lines in the bound-bound case. The bound-free absorption cross-section, σ_λ^{bf}, is defined in terms of the ionization cross-section of the hydrogen atom, $\sigma_{\lambda H}$, multiplied by a correction factor known as the Gaunt factor (GF). Thus,

$$\sigma_{\lambda,i}^{bf} = GF_{\lambda,i}\sigma_{\lambda H} \tag{2.17}$$

As a photon can stimulate a transition from all bound electronic states, the net bound-free absorption coefficient can be written as

$$\kappa_{\lambda}^{bf}(\underline{\phi}) = \sum_{i=1}^{l} \sigma_{\lambda,i}^{bf} n_i(\underline{\phi}) \tag{2.18}$$

where l is the total number of electronic states from which transitions to a free state are considered[43], $l = 14$ out of 22 levels for N and $l = 15$ out of 19 levels for O. The bound-free emission coefficient is defined as

$$\varepsilon_{\lambda}^{bf}(\underline{\phi}) = \sum_{i=1}^{l} \sigma_{\lambda,i}^{bf} n_i(\underline{\phi}) I_{b\lambda,i}^{bf}(\underline{\phi}) \tag{2.19}$$

where $I_{b\lambda,i}^{bf}(\underline{\phi})$ is the Planck function defined between a bound state and a free state as a function of electronic temperature $T_{elec,i}$,

$$I_{b\lambda,i}^{bf}(\underline{\phi}) = \frac{2hc^2}{\lambda^5} \frac{1}{e^{C_2/\lambda T_{elec,i}} - 1} \tag{2.20}$$

$$T_{elec,i} = \frac{C_2(E_\infty - E_i)}{log(n_i/n_{iE}) + C_2(E_\infty - E_i)/T_e} \tag{2.21}$$

where n_{iE} is the population of the electronic state i in equilibrium with electrons at electron temperature T_e, and is given by the Saha equation

$$n_{iE} = 2.07 \times 10^{-16} \frac{n_{q^+} n_e}{Q_+^e T_e^{1.5}} \exp\Big(- \frac{C_2 E_i}{T_e} \Big) \tag{2.22}$$

where n_{q^+} is the population of ions of specie q and Q_+^e is the ion partition function. The free-free radiation occurs as a consequence of acceleration or deceleration of an electron in the vicinity of an ion. The free-free absorption coefficients is also defined in terms of hydrogenic free-free cross section, and can be given as

$$\kappa_{\lambda}^{ff}(\underline{\phi}) = n_{q^+} n_e \sigma_{\lambda H}^{ff}(1 + d) \tag{2.23}$$

where d is a correction factor for the free-free cross-section of nonhydrogenic atomic species. Finally, the free-free emission coefficient is evaluated as

$$\varepsilon_{\lambda}^{ff}(\underline{\phi}) = \kappa_{\lambda}^{ff}(\underline{\phi}) I_{b\lambda}^{ff} = \kappa_{\lambda}^{ff}(\underline{\phi}) \frac{2hc^2}{\lambda^5 [e^{c_2/\lambda T_e} - 1]} \tag{2.24}$$

2.4 Nonequilibrium and the Quasi Steady State Assumption

In a chemical process, chemical equilibrium implies that, if left alone, there is no net change in the concentrations of the reactants and the products over time. In other words, this would be the state that results if the forward chemical process proceeds at the same rate as the reverse reaction. Similarly, a thermal equilibrium is implied when an ideal gas distribution function has stabilized to a specific Maxwell-Boltzmann distribution. If the process is very slow, it can be approximated by a sequence of equilibrium states. How-

ever, if the process is happening very fast, there may be significant departure from the equilibrium. If the characteristic time for chemical reactions in the shock-layer is comparable to the time of flight for a fluid element to pass the body, the flow is in chemical nonequilibrium. This happens at high altitudes , where the decrease of free-stream density causes an increase in chemical reaction time; and at high velocities, where the time of flight to pass the body is very small. The increase in temperature in the shock-layer triggers electronic and ro-vibrational excitations that lead to thermal nonequilibrium. The time required for the shock-layer gas to reach equilibrium strongly dependens on the pressure in the shock-layer. For example, even at very low free-stream density and extremely high velocities, the shock-layer of Galileo probe was in equilibrium due to very high pressures in the shock-layer [12].

As a consequence of nonequilibrium, the population distribution among the energy levels may be significantly different from the Boltzmann distribution. In general, though not always true, there are more particles in the higher energy levels under nonequilibrium than normally predicted by equilibrium theory, as shown in Fig. 2.5. This is due to slower de-excitation processes in low-density shock-layers. This difference in population distribution results in a very different absorption pattern, and has a great consequence on radiative heat loads.

It was found that radiative predictions based on the equilibrium model agreed well with the radiation data measured from FIRE vehicles at low altitude; however, there was considerable disagreement between the measured and the predicted values at high altitudes. This was attributed to the nonequilibrium state in the less dense air. A comparison of the radiative heat flux for the Stardust stagnation line flow field is given in Fig. 2.6, showing significant under-prediction of the heat flux values by the Boltzmann-distributed equilibrium case.

In contrast to the Earth's atmosphere, in Titan's atmosphere a Boltzmann distribution assumption for the CN electronic states may lead to an over-prediction of radiative intensities by a factor of about 3-7, as observed by Bose *et al.* [22]. Bose *et al.* also corroborated their finding by shock-tube experiments. Similar results were observed by Johnston *et al.* [60] for the Huygens probe.

In the case of equilibrium, translational, electronic, rotational and vibrational degrees of freedom are all populated according to the Boltzmann distribution, defined by one common temperature. The Boltzmann distribution is given as

$$n_i = \frac{n}{Q} e^{-C_2 E_i / T} \tag{2.25}$$

where n is the total population of the species, Q is the partition function, $C_2 = hc/k = 1.43879$ [cm K] is the second radiation constant, E_i[cm^{-1}] is the energy of the i^{th} state. The partition function is given by

$$Q = \sum_{i=1}^{M} g_i e^{-C_2 E_i / T} \tag{2.26}$$

where M is the total number of energy levels. Calculation of populations by Boltzmann distribution is a simple process; however, it can lead to very unreliable results. In contrast, prediction of nonequilibrium populations is a complicated process. The calculations require modeling of different radiative and collision processes [43]. Simplifications are often made to make the process tractable. Olynick *et al.* [2] found that the population of various vibrational and electronic states could be characterized by a

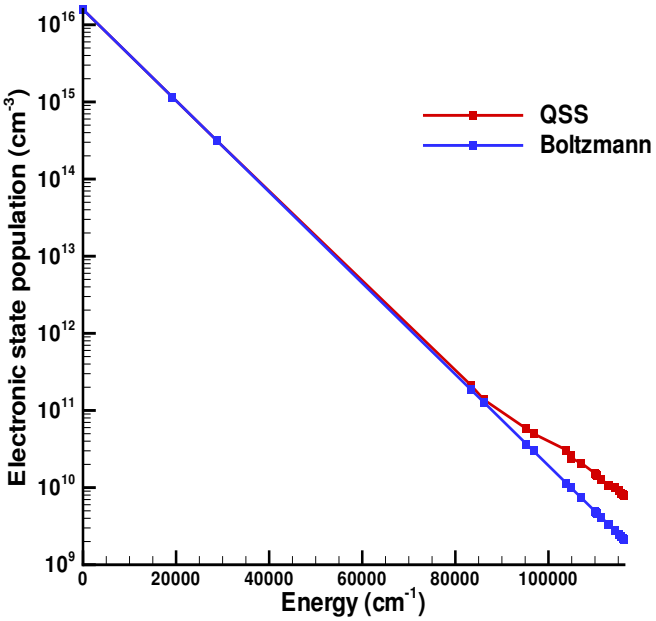

Figure 2.5. Comparison of the QSS population with the Boltzmann population for N; $n_N = 5.0 \times 10^{16}$ cm^{-3}, $n_{N^+} = 5.0 \times 10^{14}$ cm^{-3}, $n_e = 5.0 \times 10^{15}$ cm^{-3}, T_e = 10000K, T= 15000K

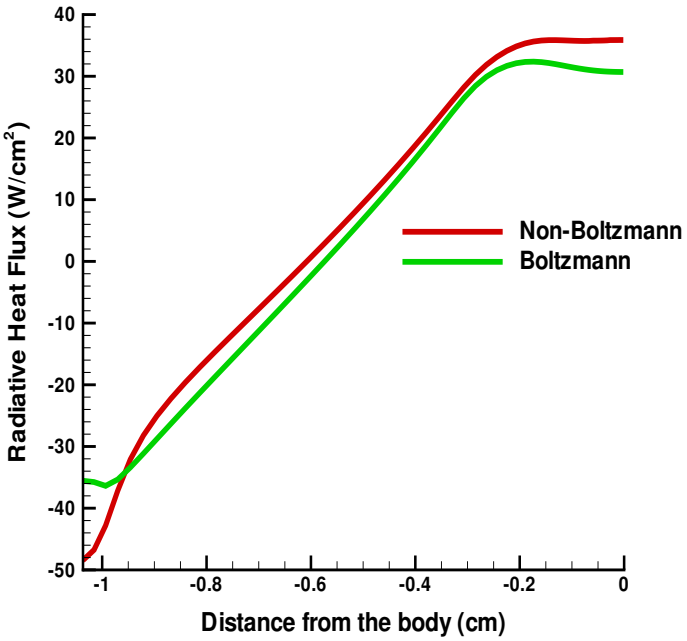

Figure 2.6. Comparison of radiative heat flux for the Stardust stagnation line flow-field: Boltzmann vs. non-Boltzmann

Boltzmann distribution at the vibrational temperature. Gally *et al.* [38, 39] developed two approximate nonequilibrium atomic radiation models, which were implemented in RAD/EQUIL, to account for the non-Boltzmann population of atomic electronic states. The first model, known as the 1st order local thermodynamic nonequilibrium (LTNE) model, assumed that the excited atomic states were in equilibrium with the ions and electrons, instead of with the ground electronic state of the atom. Thus, in this model the three lowest levels were assumed to be in a Boltzmann distribution with the ground state and the upper levels were assumed to be in a Saha-Boltzmann distribution. However, the Saha distribution may not be a valid approximation in the cold boundary-layer region. In a later improvement Gally *et al.* proposed a 2nd order LTNE model, where they divided atomic nitrogen into two fictitious species representing the first three low-lying energy states and higher energy states, respectively. The electronic states of each of the two species were assumed to be in a Boltzmann distribution at electron temperature T_e. Gally *et al.* also proposed similar approximate models for nonequilibrium molecular excitation.

The most popular and extensive method for modelling nonequilibrium populations is based on the Quasi Steady State Model (QSS) of Park [84]. The QSS condition states that the sum of all rates of transitions into an internal state (inflow rates) are equal to the sum of all rates of transitions out of the state (outflow rates). The inflow rates and outflow rates include all possible transitions, i.e., those by electrons-impact, by heavy particles impact, and by radiation. This method of finding nonequilibrium populations is also known as the collision–radiative model. For the purpose of calculating the non-Boltzmann distribution of electronic state populations in an atom, a number of energy levels are usually grouped together to form composite states. This Park model for atomic species includes 22 levels for N and 19 levels for O. An assessment of the QSS model was presented by Sharma *et al.* [89], emphasizing the need to expand the QSS model to include more energy levels, instead of composite energy levels. Similar suggestions were made by Johnston [40]. However, this can only be done at the expense of computational efficiency.

Other collision–radiative models include the Kunc and Soon model [90, 91], which includes 14 levels for N and 9 levels for O. In comparison to the Park Model [84], the collision-radiative model of Soon and Kunc uses more recent data of absorption cross-sections and Einstein coefficients. More recently, Johnston [40] has developed a very comprehensive CR model for air species, which is part of the HARA code developed by him. Johnston's model has been validated by experimental data at a number of flight conditions. As CN radiation is very significant in a number of applications, an effort was made to develop a CR model for CN bands. Bose *et al.* [22] formulated a simple CR model for CN, which provides closer agreement with experimental results as compared to Boltzmann distribution.

In this work, the database developed by Sohn *et al.*[43] is used to predict nonequilibrium populations of different electronic states. This database employs an efficient databasing scheme based on the Park model [84] to quickly determine the electronic state populations through interpolation.

Chapter 3

Correlated-*k* Distributions

In *k*-distributions the rapidly-varying spectral absorption coefficient is reordered into a monotonically increasing function over a narrow-band, part spectrum or full spectrum. Most *k*-distribution methods to date have been developed for the case of thermodynamic equilibrium, where the radiation field is represented by a single temperature. When the state of a gas in not in thermodynamic equilibrium, it cannot be described by a single temperature. The formulation of the *k*-distribution method for nonequilibrium is quite similar to its equilibrium counterpart. To understand the various adaptations of FSK methods, it is essential to have a grasp of the basic formulation of the method.

3.1 Full-Spectrum *k*-Distribution Method

Under nonequilibrium conditions, the radiative transfer equation (RTE) for an absorbing and emitting hypersonic plasma can be written as [52]

$$\frac{dI_\lambda}{ds} = \kappa_\lambda(\underline{\phi})[I^{ne}_{b\lambda}(\underline{\phi}) - I_\lambda] \tag{3.1}$$

Eq. (3.1) is reordered into a *k*-distribution by multiplying it with the Dirac-delta function $\delta(k - \kappa_\lambda(\underline{\phi}_0))$, followed by integration over the entire spectrum. Here $\kappa_\lambda(\underline{\phi}_0)$ is the absorption coefficient evaluated at some reference state $\underline{\phi}_0$. This leads to

$$\frac{dI_k}{ds} = k^*(\underline{\phi}, k)[f(\underline{\phi}, \underline{\phi}_0, k)I^{ne}_b(\underline{\phi}) - I_k] \tag{3.2}$$

provided that at every wavelength across the entire spectrum, where $\kappa_\lambda(\underline{\phi}_0) = k$, we must also have a unique value for $\kappa_\lambda(\underline{\phi}) = k^*(\underline{\phi}, k)$ everywhere within the medium. In Eq. (3.2) I_k and f are defined as

$$I_k = \int_0^\infty I_\lambda \delta(k - \kappa_\lambda(\underline{\phi}_0))d\lambda \tag{3.3}$$

$$f(\underline{\phi}, \underline{\phi}_0, k) = \frac{1}{I_b^{ne}} \int_0^\infty I_{b\lambda}^{ne}(\underline{\phi}) \delta(k - \kappa_\lambda(\underline{\phi}_0)) d\lambda \tag{3.4}$$

where f is the Planck function-weighted full spectrum k-distribution, which depends on reference state conditions $\underline{\phi}_0$ and local conditions $\underline{\phi}$. The total intensity I can be obtained by integrating I_k over the reordered k-space. The k-distribution can be considered as a probability density function (PDF), giving the probability that the absorption coefficient will attain a value k. The k-distribution f has very erratic behavior and integration in k-space is very inconvenient. However, Eq. (3.2) can be transformed into the much smoother g-space by dividing it by the k-distribution at the reference state $f(\underline{\phi}_0, \underline{\phi}_0, k)$, leading to

$$\frac{dI_g}{ds} = k^*(\underline{\phi}_0, \underline{\phi}, g)[a(\underline{\phi}, \underline{\phi}_0, g) I_b^{ne}(\underline{\phi}) - I_g] \tag{3.5}$$

with

$$I_g = I_k / f(\underline{\phi}_0, \underline{\phi}_0, k) = \int_0^\infty I_{b\lambda}^{ne}(\underline{\phi}) \delta(k - \kappa_\lambda(\underline{\phi}_0)) d\lambda \Big/ f(\underline{\phi}_0, \underline{\phi}_0, k) \tag{3.6}$$

where, g is the cumulative k-distribution and $a(\underline{\phi}, \underline{\phi}_0, g)$ is a weight or nongray stretching function given by

$$g(\underline{\phi}_0, \underline{\phi}_0, k) = \int_0^k f(\underline{\phi}_0, \underline{\phi}_0, k) dk \tag{3.7}$$

$$a(\underline{\phi}, \underline{\phi}_0, g) = \frac{f(\underline{\phi}, \underline{\phi}_0, k)}{f(\underline{\phi}_0, \underline{\phi}_0, k)} = \frac{dg(\underline{\phi}, \underline{\phi}_0, k)}{dg(\underline{\phi}_0, \underline{\phi}_0, k)} \tag{3.8}$$

In numerical calculations it is difficult to evaluate the ratio of the k-distributions f, due to their erratic behavior (having singularities at each minimum and maximum of the absorption coefficient[69]); it is much more convenient to evaluate the derivative dg/dk, as indicated in Eq. (3.8).

Because atomic lines are spread over only a very small part of the spectrum, most of the k-distribution lies in the g-range $0.99 \leq g \leq 1$. Thus, for numerical precision reasons, it is preferable to redefine the cumulative k-distribution as

$$g'(\underline{\phi}, k) = 1 - g(\underline{\phi}, k) = \int_k^{k_{max}} f(\underline{\phi}_0, \underline{\phi}_0, k) dk \tag{3.9}$$

i.e., a monotonically *decreasing* function.

The formulation of the correlated-k method for a mixture with contributions from atomic lines and continuum is exactly the same, again the only difference is in the definition of the Planck function, which, for a mixture, can be defined in terms of emission and absorption coefficient as

$$I_{b\lambda}^{ne}(\underline{\phi}) = \frac{\varepsilon_\lambda(\underline{\phi})}{\kappa_\lambda(\underline{\phi})} = \frac{\varepsilon_\lambda^{bb}(\underline{\phi}) + \varepsilon_\lambda^{cont}(\underline{\phi})}{\kappa_\lambda^{bb}(\underline{\phi}) + \kappa_\lambda^{cont}(\underline{\phi})} \tag{3.10}$$

A sample absorption spectrum of atomic N is shown in Fig. 3.1, along with the smoothly varying reordered absorption coefficient as a function of artificial wavenumber g. Since the k vs g dependence is very smooth, spectral integration of RTE in this reordered spectral space is very simple, requiring only a few quadrature points.

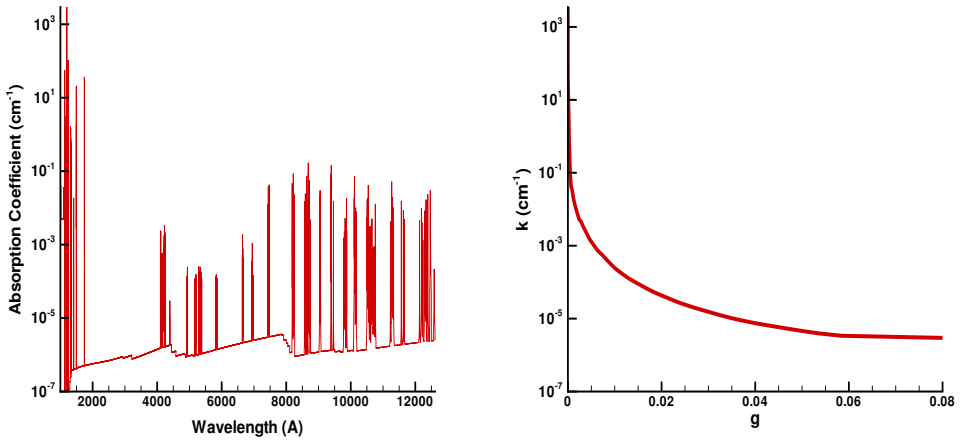

Figure 3.1. Absorption Spectrum of N (left) and corresponding k-distribution (right); $n_N = 5.0 \times 10^{16}$ cm^{-3}, $n_{N^+} = 1.0 \times 10^{16}$ cm^{-3}, $n_e = 2.0 \times 10^{16}$ cm^{-3}, T$_e$ = 10000K

3.2 Reference State

In principle, the choice of reference state is irrelevant for a truly correlated k-distribution. However, since real k-distributions are not perfectly correlated, the choice of a proper reference state can have significant impact on overall solution accuracy. For the case of thermal equilibrium Modest and Zhang [68] have suggested a reference state based on volume-averaged mole fraction and Planck-mean temperature based on average emission from the volume. For the problem of nonequilibrium atomic radiation we adopt a similar approach to evaluate the reference state. The radiation process in a hot plasma is dominated by electron collisions. Therefore, the electron temperature is the most important parameter. The Planck function for the nonequilibrium case depends on electron temperature through electronic state populations. The electron temperature for the reference state is taken as the Planck-mean temperature based on average emission from the volume. Translation temperature only affects Doppler broadening, and its value for the reference state $\underline{\phi}_0 = (T_0, T_{e0}, \underline{N}_0)$ is chosen as the volume average.

$$\underline{N}_0 = \frac{1}{V}\int_V \underline{N} dV \tag{3.11}$$

$$T_0 = \frac{1}{V}\int_V T dV \tag{3.12}$$

$$\kappa_P(\underline{\phi}_0) I_b^{ne}(\underline{\phi}_0) = \frac{1}{V}\int_V \kappa_P(\underline{\phi}) I_b^{ne}\left(\underline{\phi}\right) dV \tag{3.13}$$

where $\kappa_P(\underline{\phi})$ is the Planck-mean absorption coefficient and is given by

$$\kappa_P(\underline{\phi}) = \frac{1}{I_b^{ne}(\underline{\phi})}\int_0^\infty \kappa_\lambda(\underline{\phi}) I_{b\lambda}^{ne}\left(\underline{\phi}\right) d\lambda \tag{3.14}$$

For all the different cases of nonequilibrium atomic radiation that were considered in this thesis, this reference state provides excellent accuracy. However, it is should be tested for many more flow conditions and radiation environments.

3.3 Application of FSCK Method to Two-Cell Problem

In this section, the correlated-k method is applied to a simple two-cell problem. More severe inhomogeneous conditions of temperature and concentration are taken than actually present in typical hypersonic shock-layers. We consider two cells, each 1 cm thick, bounded by cold black walls. An example for the conditions in the two cells is given in Table 3.1. These conditions have been appropriately chosen from actual shock-layer conditions. Such two-cell problems with typical conditions serve as an acid test for the method, because of their abrupt step-change in conditions. In actual applications gradients are much more benign and the accuracy of the correlated-k method can be expected to be better. In this example radiation from only bound-bound lines is considered. Figure 3.4 shows the k-distributions for N and O for the conditions in Table 3.1. Here $\underline{\phi}_1$ represents the gas state in Cell 1 and $\underline{\phi}_2$ represents the gas state in Cell 2. $k(\underline{\phi}_1, \underline{\phi}_2, g_1)$ is the k-distribution for absorption coefficients at state $\underline{\phi}_2$ and the Planck function at state $\underline{\phi}_1$. The effect of varying the Planck function on the k-distributions can be understood in terms of stretching of k in g-space. In Fig. 3.4 this stretching is represented by lines AB and CD. For exactly correlated k-distributions the magnitude of stretching in g-space would be the same for all flow conditions, and the lines ABCD should form a rectangle. It is clear from this figure that for such highly nonhomogeneous and nonequilibrium gas conditions k-distributions are correlated neither for N nor O.

In Table 3.2 the heat fluxes coming out of the cold cell are compared. The full-spectrum k-distribution method gives reasonably accurate results for both atomic species. Even for these extreme case of inhomogeneity, the maximum error is limited to 5-7%. More accurate results can be obtained by improving the correlatedness among absorption coefficients. This is done by sorting the absorption coefficients into a number of groups, where absorption coefficients have better correlation. The grouping scheme for atomic lines will discuused in Chapter 4. In Table 3.2 the heat flux results for the mixture of N and O are also compared. The total heat flux from the mixture is found to be almost exactly equal to the sum of the indvidual gas contributions, indicating that the effect of overlap between N and O lines is not significant.

3.4 Stardust Reentry Problem

The correlated-k method is applied to the solution of the RTE in actual flow conditions. The peak heating stagnation-line flow-field of the Stardust reentry vehicle is taken. Number densities and temperature profiles for this flow-field are shown in Fig. 2.1. In Fig. 3.5 and 3.6 the local heat flux and its divergence (i.e., the radiative source in the energy equation), respectively from an N and O mixture (including continuum radiation) along the stagnation line are compared. The full-spectrum k-distribution method provides reasonably accurate results, with errors between 6-7% in the wall heat flux. Errors are slightly higher in the unimportant free-stream region, due to population inversions predicted by the QSS model, resulting in a total breakdown of correlation among absorption coefficeints.

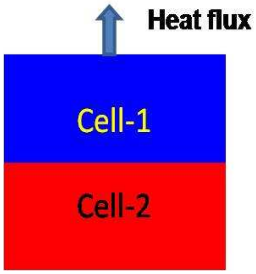

Figure 3.2. A schematic of a two-cell problem

	Cell 1	Cell 2
T, K	15011.3	24343.6
T_e, K	8578.3	19009.8
N, /cm^3	3.41×10^{16}	2.05×10^{16}
N^+, /cm^3	2.71×10^{15}	1.36×10^{15}
O, /cm^3	1.12×10^{16}	6.75×10^{15}
O^+, /cm^3	2.12×10^{11}	8.91×10^{13}
N_e, /cm^3	3.10×10^{15}	2.09×10^{15}
Thickness, cm	1.0	1.0

Table 3.1. Flow conditions for the two cells

	line-by-line	correlated-k	error
N	204.02	216.68	6.21%
O	15.61	16.47	5.56%
N + O	219.87	235.61	7.16%

Table 3.2. Heat flux exiting the cold cell (W/cm^2)

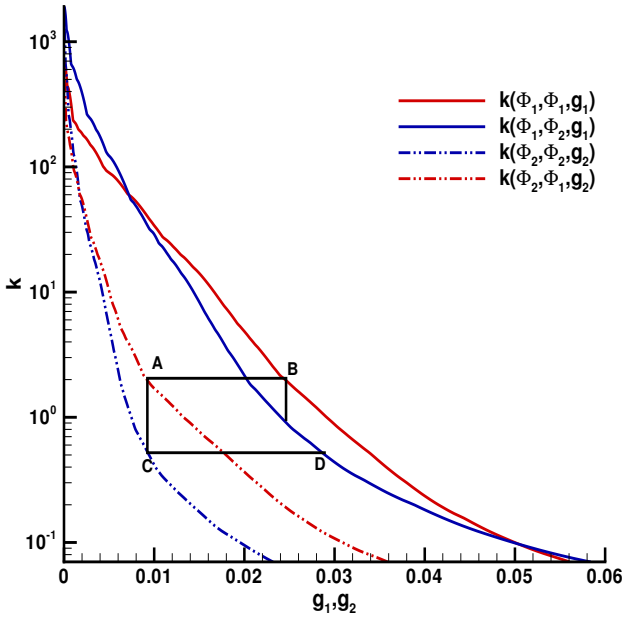

Figure 3.3. Comparison of *k*-distributions of N for conditions given in Table 3.1

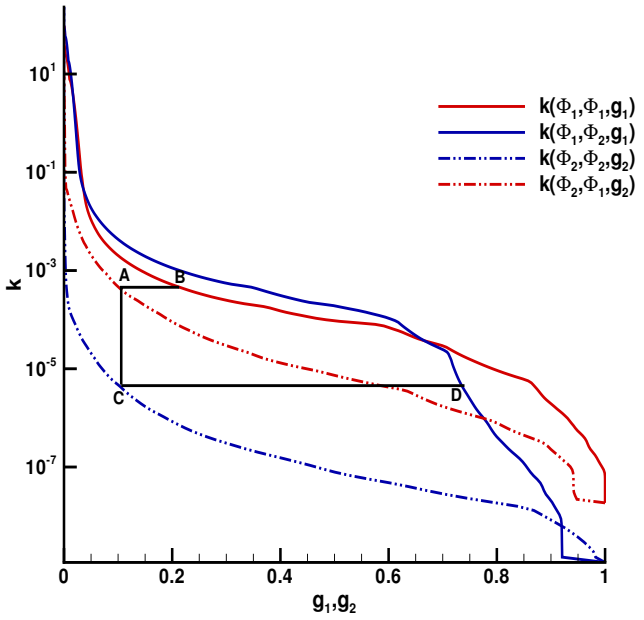

Figure 3.4. Comparison of *k*-distributions of O for conditions given in Table 3.1

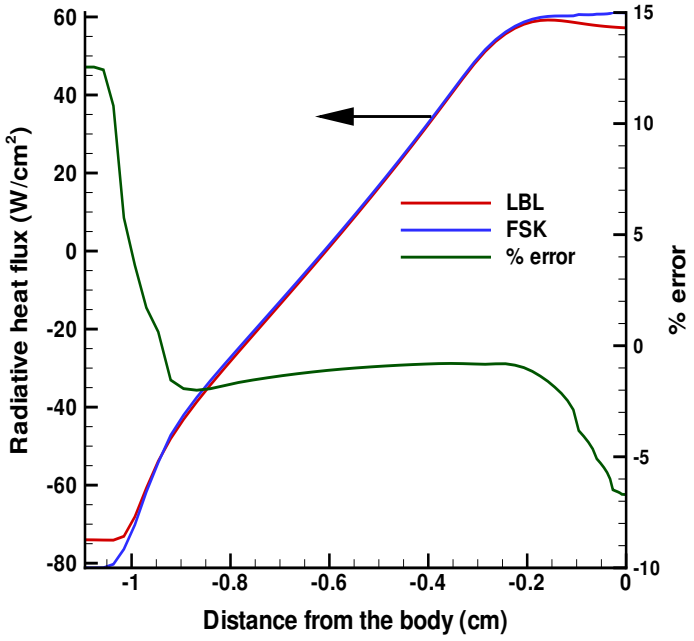

Figure 3.5. Comparison of heat flux along the stagnation line of the Stardust peak heating flow-field

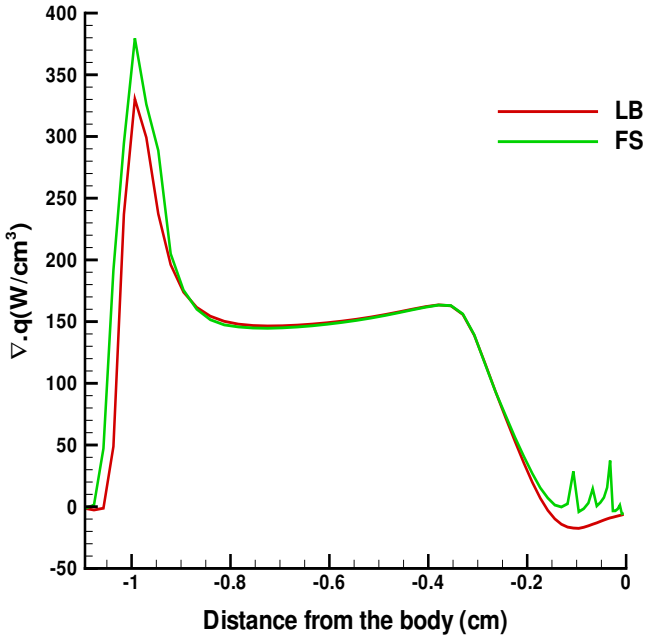

Figure 3.6. Comparison of divergence of heat flux along the stagnation line of the Stardust peak heating flow-field

Chapter 4

Multi-Group *k*-Distributions

The *k*-distribution method is exact for a homogeneous medium and for truly correlated absorption coefficients. For the case of hypersonic nonequilibrium flow large temperature and concentration gradients are present within the shock-layer, and for such a case atomic lines appear not to be well correlated. Results presented in Chapter 3 can be improved by employing a grouping scheme discussed in this chapter. Absorption coefficients of atomic lines and the nonequilibrium Planck function, as defined in Eq. (3.10), depend on the populations of upper and lower electronic states. At higher temperatures the upper states of the atom become more and more populated. Atomic lines resulting from transitions from any of these upper states become stronger in high temperature regions. The line strength strongly depends on electron temperature. The dependence of absorption line strengths on electron temperature for few selected atomic lines N and O are plotted in Fig. 4.1 and 4.2, respectively. It can be observed from this figures that different atomic lines have distinct patterns of dependence on electron temperature. It can also be observed that lines plotted in the same color show similar behavior (red lines show a continuous gradual decay of line strength with electron temperature; blue lines continuously increase with temperature; green lines first decrease slightly, then strongly increase with temperature; and, finally, black lines first decrease with temperature before rising again gradually). All bound-bound lines of N and O have behavior similar to one or the other of these selected lines. This dependence is plotted for just one value of neutral, ion and electron populations. For different values of populations the dependence is quite similar. The distinct behavior of these atomic lines in different flow conditions results in uncorrelatedness between the *k*-distributions. Zhang and Modest [79] have shown that dividing the spectrum into different spectral groups, according to their absorption coefficient dependence on gas conditions, greatly improves the accuracy of the correlated-*k* method. We adopt a similar approach for the case of atomic lines. Transitions shown in the same color can be combined or put into the same group.

All 170 lines of N can be sorted into three different non-overlapping spectral groups, and similarly, all the 86 O lines can be sorted into 4 different spectral groups. These spectral groups for N and O are shown in Figs. 4.3 and 4.4, respectively. It is also possible to combine similar groups of N and O, provided that separate groups do not overlap with each other. It can be observed from Figs. 4.3 and 4.4 that N and O groups, shown in the same color, have similar dependence on electron temperature, and, therefore, can

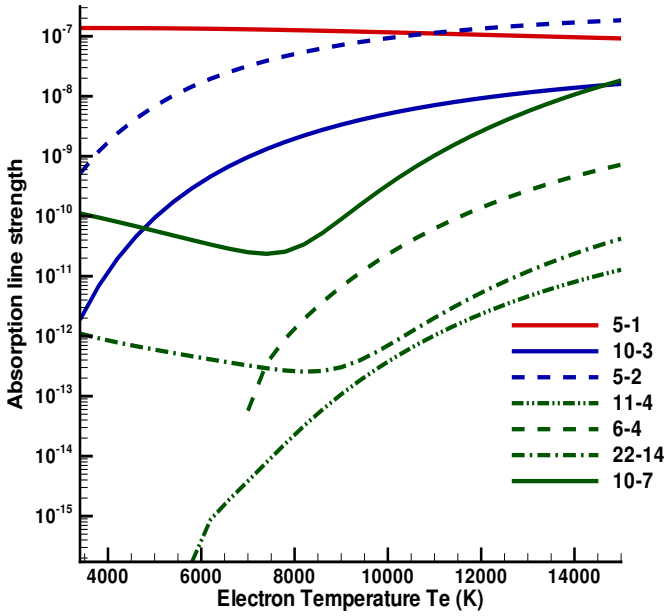

Figure 4.1. Dependence of absorption line strength of atomic N on electron temperature

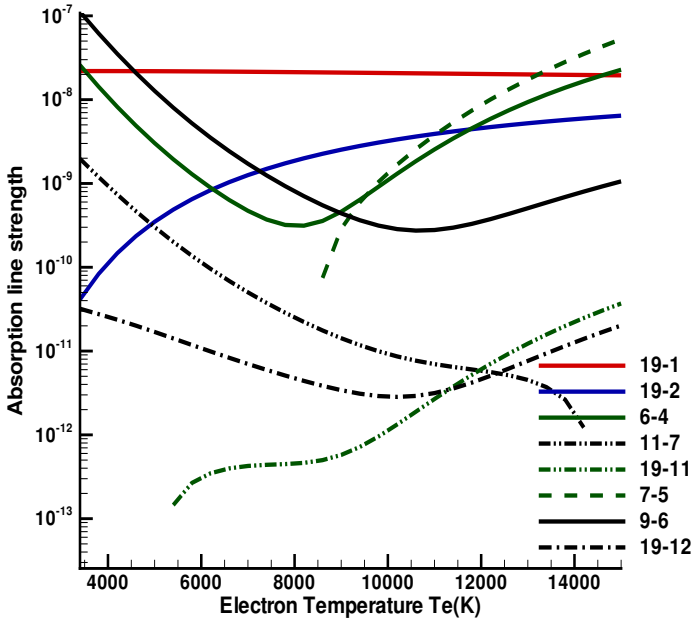

Figure 4.2. Dependence of absorption line strength of atomic O on electron temperature

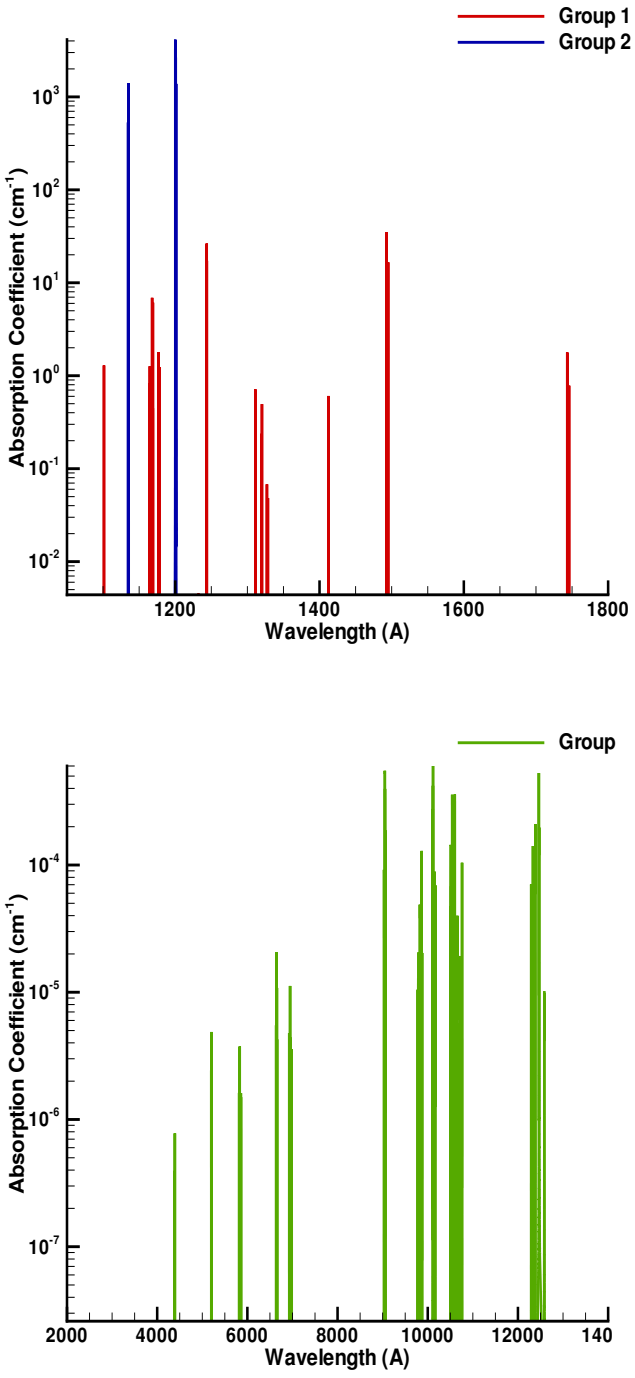

Figure 4.3. Spectral groups of atomic lines of N

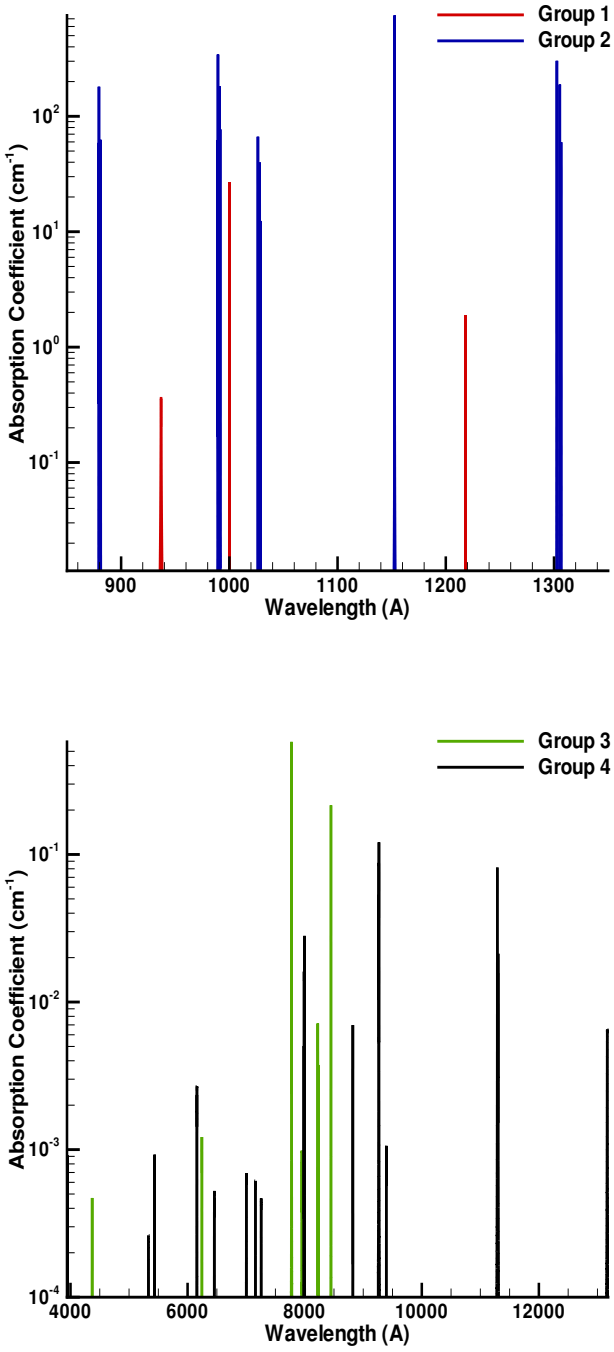

Figure 4.4. Spectral groups of atomic lines of O

be combined together. Thus, we can reduce the total number of groups to four, each shown in a different color. Also, continuum radiation from both species can be modelled as a single separate group. Thus, the total spectrum for N and O mixtures can be divided into 5 groups.

4.1 Theoretical Formulation of Multi-Group *k*-Distribution Model

The correlated-k method for the multi-group case can essentially be developed in the same way as for the full spectrum [79]. If we divide the full spectrum into M different part-spectra, each containing one group, then for the m-th group, multiplying Eq. (3.1) by the Dirac-delta function $\delta(k_m - \kappa_\lambda(\lambda, \underline{\phi}_0))$, followed by integration across the m-th spectral group leads to

$$\frac{dI_{km}}{ds} = k(\underline{\phi}, k_m)[f_m(\underline{\phi}, \underline{\phi}_0, k_m)I_b^{ne}(\underline{\phi}) - I_{k_m}] \tag{4.1}$$

where

$$I_{km} = \int_{\lambda\in[\lambda_m]} I_\lambda \delta(k_m - \kappa_\lambda(\lambda, \underline{\phi}_0))d\lambda \tag{4.2}$$

$$f_m(\underline{\phi}, \underline{\phi}_0, k_m) = \frac{1}{I_b^{ne}} \int_{\lambda\in[\lambda_m]} I_{b\lambda}^{ne}(\lambda, \underline{\phi})\delta(k_m - \kappa_\lambda(\lambda, \underline{\phi}_0))d\lambda \tag{4.3}$$

Here f is the Planck function-weighted full spectrum k-distribution for the m-th group, which depends on reference state conditions $\underline{\phi}_0$ and local conditions $\underline{\phi}$. Similar to the single group case, Eq. (4.1) can be transformed into the much smoother g-space, leading to

$$\frac{dI_{gm}}{ds} = k^*(\underline{\phi}_{0,m}, \underline{\phi}, g_m)[a_m(\underline{\phi}, \underline{\phi}_0, g_m)I_b^{ne}(\underline{\phi}) - I_{gm}] \tag{4.4}$$

with

$$I_{gm} = I_{km}/f_m(\underline{\phi}_0, \underline{\phi}_0, k_m) \tag{4.5}$$

$$g_m(\underline{\phi}_0, \underline{\phi}_0, k_m) = \int_0^{k_m} f_m(\underline{\phi}_0, \underline{\phi}_0, k_m)dk_m \tag{4.6}$$

$$a(\underline{\phi}, \underline{\phi}_0, g_m) = \frac{f_m(\underline{\phi}, \underline{\phi}_0, k_m)}{f_m(\underline{\phi}_0, \underline{\phi}_0, k_m)} = \frac{dg_m(\underline{\phi}, \underline{\phi}_0, k_m)}{dg_m(\underline{\phi}_0, \underline{\phi}_0, k_m)} \tag{4.7}$$

The total intensity I can then be obtained by integrating I_{gm} over the reordered g-space and summing over all spectral groups, i.e.,

$$I = \sum_{m=1}^{M} \int_0^{g_{m,max}} I_{gm} dg_m \tag{4.8}$$

$$\sum_{m=1}^{M} g_{m,max} = 1 \tag{4.9}$$

4.2 Application of the Multi-Group *k*-Distribution Method to Heat Transfer Calculations

In Chapter 3, heat transfer results for the two-cell problem and the Stardust Stagnation line flow-field were discussed for the single group (full-spectrum) case. In this chapter, results for the same problems are presented with the grouping scheme and compared with the single group case, as well as line-by-line bench-marks.

In Table 4.1, heat fluxes coming out of the cold cell are compared for bound-bound lines of N and O. It is clear that there is significant improvement in the accuracy of the correlated-*k* method once atomic lines are grouped according to their absorption characteristics. For both N and O the error reduces to below 2%. It is also observed that 4-group model for the mixture of N and O also gives very good agreement with line-by-line results.

In Fig. 4.5 and 4.6 local heat flux and its divergence for a mixture of N and O (including atomic continua) are compared for the Stardust flow-field. Although the single-group model is fairly accurate, there is significant improvement in the shock-layer and the colder boundary-layer regions, this is due to population inversions predicted by QSS in these regions that results in a total breakdown of correlation for the full spectrum case. The agreement is excellent between the 5-group correlated-*k* model (continua treated separately as the 5th group) and the line-by-line results. There is $2-3\%$ error in the radiative heat flux onto the spacecraft for the case of 5-groups, while the single-group method has an error of $6-7\%$. The maximum error along the stagnation line is found to be 5% for the case of 5-groups, while the single group approach has a maximum error of 12% in the free stream.

	line by line		correlated-*k*	error
N	204.02	1 group	216.68	6.21%
		3 groups	200.25	1.85%
O	15.61	1 group	16.47	5.56%
		4 groups	15.71	0.63%
N + O	219.87	1 group	235.61	7.16%
		7 groups	215.96	1.77%
		4 groups	215.51	1.98%

Table 4.1. Heat flux exiting the cold cell (W/cm^2) for multi-group model

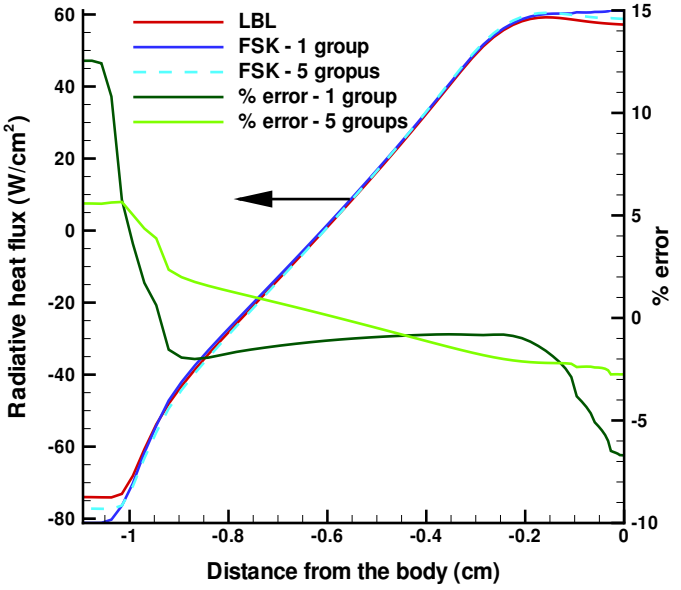

Figure 4.5. Heat flux along the Stardust stagnation-line flow-field for multi-group model

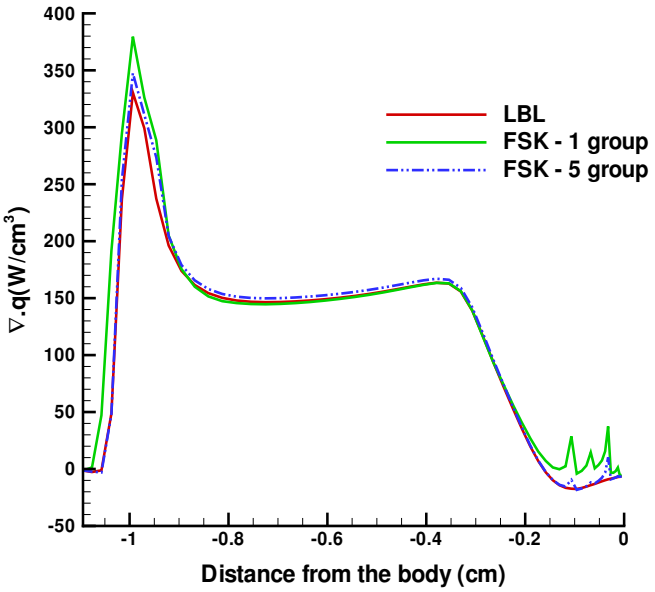

Figure 4.6. Divergence of heat flux along the Stardust stagnation-line flow-field for multi-group model

Chapter 5

k-Distribution Database

The FSCK and multi-group FSCK approaches make it possible to evaluate radiative fluxes at a fraction of the cost needed by line-by-line methods. However, considerable preparatory work is required before the method can be used: (i) determination of the spectral absorption coefficient for all flow conditions, and (ii) assembly of *k*-distributions from the absorption coefficients. A number of simple parametric correlations have been proposed for fast evaluation of the *k*-distributions [92]. While the correlation method has its limitations, it is advantageous to database *k*-distributions, from which any desired full-spectrum *k*-distribution can be calculated on-the-fly. Modest and Riazzi [93] have shown the advantages and applicability of using such a database in combustion applications. They databased a set of *k*-distributions as a function of thermodynamic state parameters. The databasing scheme was further optimized by Wang and Modest [94], who demonstrated the use of various quadrature schemes for preparing a highly accurate and compact database. In the case of nonequilibrium atomic radiation, there are a large number of parameters to database, which include translation and electron temperatures and number densities of electrons, neutral atoms and ions. The presence of such a large number of parameters complicates the databasing scheme. However, some of these difficulties can be overcome by appropriately dividing the full spectrum into a number of narrow bands. In Section 5.1, a narrow-band version of the *k*-distribution method will be developed for a mixture of N and O. In Section 5.2, a scheme for the *k*-distribution database will be developed. Finally, a procedure for constructing the full-spectrum *k*-distribution from narrow-band data will be described in Section 5.4.

5.1 Narrow-Band *k*-Distribution for Mixture of Species

The theory of the full-spectrum *k*-distribution was presented in Chapter 3. In this section, a more general formulation of the narrow-band *k*-distribution method for a mixture of N and O, including bound-bound and continuum radiation, is discussed. The RTE for an absorbing/emitting medium was given in Eq. (3.1). For a mixture the total spectral absorption coefficient, including contributions from bound-bound

lines and continuum can be written as

$$\kappa_\lambda(\underline{\phi}) = \kappa_\lambda^{bb}(\underline{\phi}) + \kappa_\lambda^{cont}(\underline{\phi}) \tag{5.1}$$

The nonequilibrium Planck function $I_{b\lambda}(\underline{\phi})$ was defined in Chapter 3, and is again presented here for convenience

$$I_{b\lambda}^q(\phi) = \frac{2hc^2}{\lambda^5}\frac{n_U^q(\underline{\phi})}{n_L^q(\underline{\phi}) - n_U^q(\underline{\phi})} = I_{b\lambda}^c X^q(\underline{\phi}), \quad q = \text{N or O} \tag{5.2}$$

where $X^q(\underline{\phi})$ is the ratio of populations, $I_{b\lambda}^c$ is the part of the Planck function, which does not depend on the gas state, and the superscript q is used to distinguish the two species N and O. Let us define another state vector $\underline{\psi}(T, T_e, n_e)$ that does not include ion and neutral number densities. Bound-bound atomic lines result from transitions from one electronic state to any other. The absorption coefficient for this case can be written as

$$\kappa_\lambda^{bb}(\underline{\phi}) = \kappa_\lambda^{cq}[n_L^q(\underline{\phi}) - n_U^q(\underline{\phi})]\Phi^q(\underline{\psi}) = \kappa_\lambda^{cq}\Delta n^q(\underline{\phi})\Phi^q(\underline{\psi}), \tag{5.3}$$

where $\Phi^q(\underline{\psi})$ is the line shape function and $\Delta n^q(\underline{\phi})$ is the difference between the lower and upper electronic state population. It can be observed from Eq. (5.3) that the nonequilibrium absorption coefficient depends on five parameters, namely, two temperatures and ion, neutral and electron number densities. Thus, a narrow-band database of k-distributions must include these five parameters. Clearly, such a database is impractical as it would require huge storage space in addition to fifth-order interpolation. However, if narrow-bands are chosen in such a way that each narrow-band contains absorption coefficients from similar lines, i.e., bound-bound atomic lines with the same n_L and n_U, the number of parameters to database can be reduced. Most atomic lines are very narrow and do not overlap with other lines, and atomic lines that do overlap have similar upper and lower electronic states. In this work it will be assumed that only similar lines overlap, giving us the freedom of choosing nonoverlapping narrow-bands. For the bound-bound case, we define a normalized absorption cross-section as

$$\kappa_\lambda^{'q}(\underline{\psi}) = \kappa_\lambda^{cq}\Phi^q(\underline{\psi}) = \frac{\kappa_\lambda^{bb}(\underline{\phi})}{\Delta n^q(\underline{\phi})} \tag{5.4}$$

In this form the absorption cross-section does not depend on the population of electronic states, and thus does not depend on number densities of neutral and ionic atomic species. k-distributions will be generated and databased for the absorption cross-section $\kappa_\lambda^{'}$ for each narrow-band. Eq. (3.1) can be rewritten in the following form

$$\frac{dI_\lambda}{ds} = [\kappa_\lambda^{bb} I_{b\lambda}^{bb} + \kappa_\lambda^{cont} I_{b\lambda}^{cont}] - [\kappa_\lambda^{bb} + \kappa_\lambda^{cont}]I_\lambda \tag{5.5}$$

The continuum absorption coefficient does not vary significantly over a narrow-band[43], and is assumed to be a constant for each narrow-band, i.e., for the m-th narrow-band $\kappa_\lambda^{cont} = \kappa_m^{cont}$. The continuum contribution does not change the nature of the k-distribution, and only scales up the k values by a constant amount for a given narrow-band. Also, for continuum radiation the Planck function cannot be specified explicitly by Eq. (5.2), and the quantity $X(\underline{\phi})$ is calculated by conserving the total continuum emission

over the narrow-band, i.e.,

$$X_m^{cont}(\underline{\phi}) = \frac{\varepsilon_m^{cont}(\underline{\phi})}{\kappa_m^{cont}(\underline{\phi}) I_{bm}^c} \tag{5.6}$$

where ε_m^{cont} is the total continuum emission from the narrow-band, and

$$I_{bm}^c = \int_{\Delta\lambda_m} \frac{2hc^2}{\lambda^5} d\lambda = \int_{\Delta\lambda_m} I_{b\lambda}^c d\lambda \tag{5.7}$$

The quantities $\Delta n^q(\underline{\phi})$, $X^q(\underline{\phi})$, $\kappa_\lambda^{cont}(\underline{\phi})$ and $\varepsilon_m^{cont}(\underline{\phi})$ are readily and efficiently calculated on-the-fly for given flow conditions (as opposed to databasing them in terms of 5 parameters, requiring lookup plus fifth-order interpolation). The theory for performing these calculations was presented in Chapter 2.

Eq. (5.5) is reordered into a k-distribution by multiplying it with the Dirac-delta function $\delta(k-\kappa_\lambda(\underline{\phi}_0))$, followed by integration over the narrow-band. $\kappa_\lambda(\underline{\phi}_0)$ is the total absorption coefficient evaluated at some reference state $\underline{\phi}_0$. For the m-th narrow-band this leads to

$$\begin{aligned}\frac{dI_{km}}{ds} =& (k_m^*(\underline{\phi}, k_m) - \kappa_m^{cont}(\underline{\phi})) \int_{\Delta\lambda_m} I_{b\lambda}^{bb}(\underline{\phi}) \delta(k_m - \kappa_\lambda(\underline{\phi}_0)) d\lambda \\ &+ \kappa_m^{cont}(\underline{\phi}) \int_{\Delta\lambda_m} I_{b\lambda}^{cont}(\underline{\phi}) \delta(k_m - \kappa_\lambda(\underline{\phi}_0)) d\lambda - k_m^*(\underline{\phi}, k_m) I_{km}\end{aligned} \tag{5.8}$$

provided that every wavelength where $\kappa_\lambda(\underline{\phi}_0)$ has one and the same value k_m, $\kappa_\lambda(\underline{\phi})$ also has one unique value $k_m^*(\underline{\phi}, k_m)$. Simplifying Eq. (5.8),

$$\begin{aligned}\frac{dI_{km}}{ds} =& k_m^*(\underline{\phi}, k_m) \Big[\int_{\Delta\lambda_m} I_{b\lambda}^{bb}(\underline{\phi}) \delta(k_m - \kappa_\lambda(\underline{\phi}_0)) d\lambda - I_{km} \Big] \\ &+ \kappa_m^{cont}(\underline{\phi}) \int_{\Delta\lambda_m} (I_{b\lambda}^{cont}(\underline{\phi}) - I_{b\lambda}^{bb}(\underline{\phi})) \delta(k_m - \kappa_\lambda(\underline{\phi}_0)) d\lambda \\ =& k_m^*(\underline{\phi}, k_m) [f_{m1}(\underline{\phi}, \underline{\phi}_0, k_m) I_{bm}(\underline{\phi}) - I_{km}] \\ &+ \kappa_m^{cont}(\underline{\phi}) f_{m2}(\underline{\phi}, \underline{\phi}_0, k_m) I_{bm}(\underline{\phi})\end{aligned} \tag{5.9}$$

where f_{m1} and f_{m2} are narrow-band k-distributions for the mixture, evaluated as follows

$$\begin{aligned}f_{m1}(\underline{\phi}, \underline{\phi}_0, k_m) &= \frac{1}{I_{bm}(\underline{\phi})} \int_{\Delta\lambda_m} I_{b\lambda}^{bb}(\phi) \delta(k_m - \kappa_\lambda(\underline{\phi}_0)) d\lambda \\ &= \frac{1}{I_{bm}(\underline{\phi})} \sum_i I_{b\lambda i}^{bb}(\underline{\phi}) \left| \frac{d\lambda}{d\kappa_\lambda} \right|_{\kappa_\lambda(\underline{\phi}_0) = k_m}\end{aligned} \tag{5.10}$$

$$\begin{aligned}f_{m2}(\underline{\phi}, \underline{\phi}_0, k_m) &= \frac{1}{I_{bm}(\underline{\phi})} \int_{\Delta\lambda_m} (I_{b\lambda}^{cont}(\underline{\phi}) - I_{b\lambda}^{bb}(\underline{\phi})) \delta(k_m - \kappa_\lambda(\phi_0)) d\lambda \\ &= \frac{1}{I_{bm}(\underline{\phi})} \sum_i (I_{b\lambda i}^{cont}(\underline{\phi}) - I_{b\lambda i}^{bb}(\underline{\phi})) \left| \frac{d\lambda}{d\kappa_\lambda} \right|_{\kappa_\lambda(\underline{\phi}_0) = k_m}\end{aligned} \tag{5.11}$$

A narrow-band may include contributions from bound-bound lines of both N and O; however, with

the assumption that there is no overlap between N and O bound-bound lines, Eq. (5.10) can be rewritten as

$$f_{m1}(\underline{\phi}, \underline{\phi}_0, k_m) = \frac{1}{I_{bm}(\underline{\phi})} \sum_{q=\mathrm{N,O}} \left[\sum_i I^q_{b\lambda i}(\underline{\phi}) \left| \frac{d\lambda}{d\kappa_\lambda} \right|^q_{\kappa_\lambda(\underline{\phi}_0)=k_m} \right] \tag{5.12}$$

where summation is over all occurrences where $\kappa_\lambda(\underline{\phi}_0) = k_m$, separately for each specie. Using Eq. (5.2) and Eq. (5.4),

$$\begin{aligned} f_{m1}(\underline{\phi}, \underline{\phi}_0, k_m) &= \frac{1}{I_{bm}(\underline{\phi})} \sum_{q=\mathrm{N,O}} \left[\frac{X^q(\underline{\phi})}{\Delta n^q(\underline{\phi}_0)} \sum_i I^c_{b\lambda i} \left| \frac{d\lambda}{d\kappa'_\lambda} \right|^q_{\kappa'^q_\lambda(\underline{\psi}_0)=k'_m} \right] \\ &= \frac{I^c_{bm}}{I_{bm}(\underline{\phi})} \sum_{q=\mathrm{N,O}} \frac{X^q(\underline{\phi})}{\Delta n^q(\underline{\phi}_0)} f'^q_m(\underline{\psi}_0, k'_m) \end{aligned} \tag{5.13}$$

In Eq. (5.13) f'^q_m is the k-distribution for the absorption cross-section κ'_λ of species q, and is defined as

$$f'^q_m(\underline{\psi}_0, k'_m) = \frac{1}{I^c_{bm}} \sum_i I^c_{b\lambda i} \left| \frac{d\lambda}{d\kappa'_\lambda} \right|^q (\underline{\psi}_0) \tag{5.14}$$

where

$$I_{bm}(\underline{\phi}) = I^c_{bm} \sum_{q=\mathrm{N,O}} X(\underline{\phi})^q \tag{5.15}$$

has been defined for convenience. Similarly,

$$f_{m2}(\underline{\phi}, \underline{\phi}_0, k_m) = \frac{I^c_{bm}}{I_{bm}(\underline{\phi})} \sum_{q=\mathrm{N,O}} \frac{X^{cont}(\underline{\phi}) - X^q(\underline{\phi})}{\Delta n^q(\underline{\phi}_0)} f'^q_m(\underline{\psi}_0, k'_m) \tag{5.16}$$

The cumulative k-distribution for a narrow-band can be defined as

$$g_m(\underline{\phi}, \underline{\phi}_0, k_m) = \int_{k_m}^{\infty} f_{m1}(\underline{\phi}, k) dk = \frac{I^c_{bm}}{I_{bm}(\underline{\phi})} \sum_{q=\mathrm{N,O}} X^q(\underline{\phi}) g'^q_m(\underline{\psi}_0, k'_m) \tag{5.17}$$

and,

$$g_{m2}(\underline{\phi}, \underline{\phi}_0, k_m) = \frac{I^c_{bm}}{I_{bm}(\underline{\phi})} \sum_{q=\mathrm{N,O}} \left(X^{cont}(\underline{\phi}) - X^q(\underline{\phi}) \right) g'^q_m(\underline{\psi}_0, k'_m) \tag{5.18}$$

For bands that do not have any contribution from bound-bound lines, $g_{m2} = H(k_m - \kappa^{cont}_m)$, where H is the Heaviside function. In Fig. 5.1 sample narrow-band k-distributions (k'_m vs g'_m) have been plotted for atomic N and O. These k-distributions have been generated for the absorption cross-section κ'_λ, and the actual k-distribution of a specie can be constructed by scaling the k'_m values as

$$k^q_m(\underline{\phi}, g_m) = \Delta n^q(\underline{\phi}) k'^q_m(\underline{\psi}, g'^q_m), \tag{5.19}$$

and, because $k^q_m(\underline{\phi})$ and $k'^q_m(\underline{\psi})$ differ by only a constant factor across a narrow-band, the cumulative k-

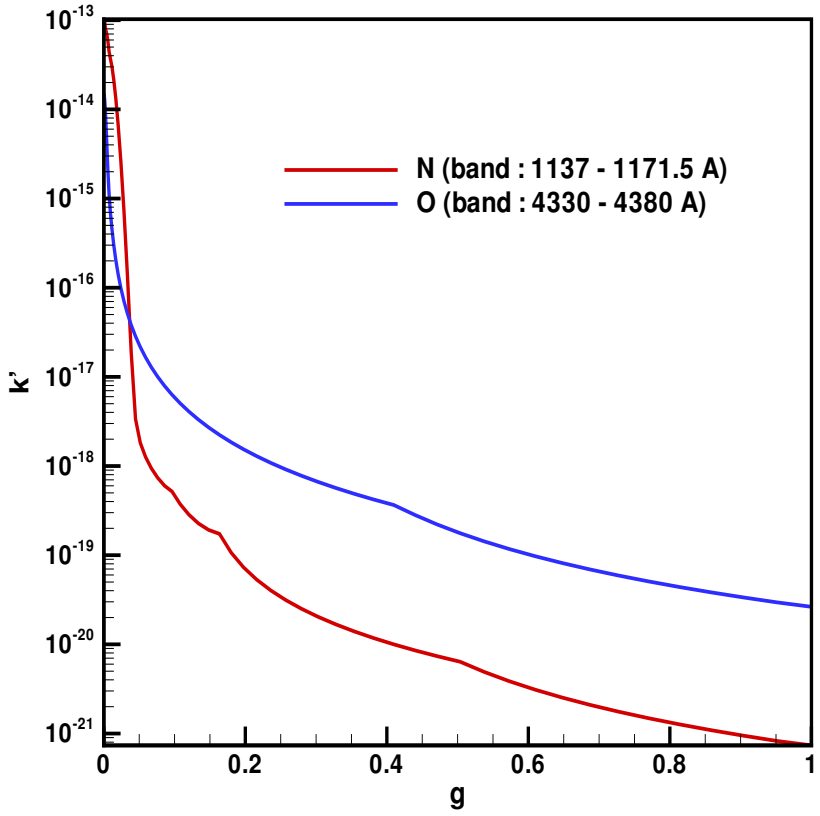

Figure 5.1. Sample narrow-band k-distributions for N and O; $n_e = 2.70 \times 10^{15}$ cm^{-3}, T$_e$ = 10000K, T= 15000K

distribution remains the same, i.e., $g_m^q(\underline{\phi}, k_m) = g_m^{'q}(\underline{\psi}, k_m^{'})$.

5.2 Database Generation

The main objective of this work is to generate and store accurate narrow-band k-distribution data as a function of three parameters; namely, T, T_e and n_e. To generate accurate k-distribution data, high-fidelity raw absorption coefficient data need to be used. In this work the database developed by Sohn *et al.*[43] was employed to calculate absorption coefficients for different flow conditions. The line shape is most realistically described by the Voigt profile. A spectral resolution of 0.001Å was used to ensure that generated k-distributions were accurate. As a first step, the full spectrum is divided into a number of narrow-band intervals. The narrow-band wavelength intervals are chosen arbitrarily in such a way that there is enough room for line broadening (ensuring that more than 99.5% of emission is captured from each line) and only lines with similar electronic transitions overlap. The Voigt line shape can become very wide in extreme conditions (large n_e and T_e values) and some narrow bands may become correspondingly

wide, and this may lead to overlap between narrow-bands. In this work the Voigt line width is limited to such a value that there is no overlap between the narrow-bands. Details of narrow-band intervals are given in Table 3 in the Appendix. The ID number of a band specifies the species contributing to that number-band. The spectrum is divided into a total of 105 narrow-bands, which include 40 narrow-bands of N, 30 narrow-bands of O and remaining narrow-bands are of continum radiation only.

The parametric conditions used to generate the k-distributions are given in Table 4 in the Appendix. It was found that more points are required for smaller values of electron number density and the two temperatures. This is achieved by selecting equally-spaced points using a power law distribution, similar to the scheme used in the Sohn *et al.* database. The absorption cross-section has a very strong dependence on the electron density n_e, and thus relatively many n_e points are needed in the database.

The next step involves generating high-accuracy k-distributions from absorption cross-section data evaluated at each of the gas conditions listed in Table 4. This involves choosing a (large) number of $k_m^{'}$-bins and calculating the cumulative k-distribution $g_m(\underline{\psi}, k_m^{'})$ for every $k^{'}$-value. We employed $\mathrm{N}_{pt} = 5000$ $k^{'}$-bins distributed according to [94],

$$\Delta(k^{\beta}) = [(k_{max})^{\beta} - (k_{min})^{\beta}]/(N_{pt} - 1) \tag{5.20}$$

$$k^{i} = [(k_{min})^{\beta} - i\Delta(k^{\beta})]^{1/\beta},\ i = 1, 2, ..., N_{pt} \tag{5.21}$$

where k_{min} and k_{max} are minimum and maximum values of the absorption cross-section $\kappa_{\lambda}^{'}$ at a given value of n_e, T_e and T. This scheme employs an exponential factor $\beta = 0.1$ to generate a skewed distribution that places more points at smaller $k^{'}$-values. A k-distribution database employing 5000 points requires vast storage space —13.5GB for all the conditions given in Table 4. Therefore, the next step is to reduce its size, without compromising accuracy. Wang and Modest [94] have described a number of schemes by which the size of the data can be reduced. This includes the concept of fixed g and storing the data using a Gaussian quadrature scheme. The k-distribution data are sets of $k^{'}$-values for sets of g_m-values, but not both need to be stored. One may fix either $k^{'}$ or g_m-values for all narrow-bands and only the other set of values needs to be in the database. Since the g_m values always vary between 0 and 1, it is more convenient to fix values of g_m. However, k-distributions are calculated for a chosen set of $k^{'}$-values, and interpolation of $k^{'}$-values at fixed g_m-values is required before storing them in the database. Following the work of Wang and Modest, a scalable Gauss-Chebyshev quadrature scheme has been used for data compaction. An n-node Gauss-quadrature scheme has $(2n-1)$-th order of accuracy. The fixed g_m-values are chosen as the abscissas of the Chebyshev polynomial of the second kind $U_n(x)$[94].

The use of the Gauss-Chebyshev quadrature scheme has one particular advantage of scalability, i.e., the lower rank quadrature is a subset of the next higher rank quadrature. In other words, for any given U_n, one can always find another U_m whose zeroes include all the zeroes of U_n. In this work, the minimum number of quadrature points used is 32 and a maximum of 128-points were used to set the fixed g_m-values. The Gauss-Chebyshev quadrature scheme puts more quadrature points at higher g_m-values. As already mentioned, it is advantageous to define a monotonically decreasing cumulative k-distribution and thus to have more quadrature points at lower g_m-values, i.e., higher $k^{'}$-values. This can be achieved by employing

a transformation as

$$g_n^{'} = (1 - g_n)^{\alpha}, \tag{5.22}$$

leading to modified quadrature weights

$$w_n^{'} = \alpha w_n (1 - g_n)^{\alpha - 1} \tag{5.23}$$

A value of $\alpha = 2.0$ places more points at smaller g-values, and has been used in this work. With this quadrature scheme the total size of the database was reduced to 170 MB for both the species.

5.3 Databasing for Continuum Properties

In Chapter 2, equations for the evaluation of bound-free and free-free emission and absorption coefficients were presented. The continuum absorption coefficient does not vary significantly over a narrow-band, and is assumed to be a constant over each narrow-band. The continuum absorption coefficient can be written as the sum of bound-free and free-free components.

$$\kappa_m^{cont}(\underline{\phi}) = \kappa_m^{bf}(\underline{\phi}) + \kappa_m^{ff}(\underline{\phi}) \tag{5.24}$$

From the theory discussed in Chapter 2, an average absorption coefficient for the m-th narrow-band is defined as

$$\kappa_m^{cont}(\underline{\phi}) = \sum_{i=1}^{l} n_i(\underline{\phi})(\sigma^{bf}_{\lambda_{start},i} + \sigma^{bf}_{\lambda_{end},i})/2 + (\kappa^{ff}_{\lambda_{start},i} + \kappa^{ff}_{\lambda_{end},i})/2 \tag{5.25}$$

$$\kappa_m^{cont}(\underline{\phi}) = \sum_{i=1}^{l} n_i \overline{\sigma}^{bf}_{m,i} + \overline{\kappa}^{ff}_m(\underline{\phi}) \tag{5.26}$$

In the database values of $\overline{\sigma}^{bf}_{m,i}$ are stored for all l levels for each narrow-band, values of $\overline{\kappa}^{ff}_m(\underline{\phi})$ are calculated on the fly. We also need to find the values of $\varepsilon_m^{cont}(\underline{\phi})$. Again we write it as a sum of bound-free and free-free components

$$\varepsilon_m^{cont}(\underline{\phi}) = \varepsilon_m^{bf}(\underline{\phi}) + \varepsilon_m^{ff}(\underline{\phi}) \tag{5.27}$$

$$\varepsilon_m^{cont}(\underline{\phi}) = \int_{\lambda_{start}}^{\lambda_{end}} \sum_{i=1}^{l} n_i(\underline{\phi}) \sigma^{bf}_{\lambda,i} I^{bf}_{b\lambda,i}(\underline{\phi}) d\lambda + \int_{\lambda_{start}}^{\lambda_{end}} \varepsilon^{ff}_{\lambda}(\underline{\phi}) d\lambda \tag{5.28}$$

$$\varepsilon_m^{cont}(\underline{\phi}) = \sum_{i=1}^{l} n_i(\underline{\phi}) \int_{\lambda_{start}}^{\lambda_{end}} \sigma^{bf}_{\lambda,i} I^{bf}_{b\lambda,i}(\underline{\phi}) d\lambda + \varepsilon^{ff}_m(\underline{\phi}) \tag{5.29}$$

$$\varepsilon_m^{cont}(\underline{\phi}) = \sum_{i=1}^{l} n_i(\underline{\phi}) \overline{\varepsilon}^{bf}_m(\underline{\phi}) + \varepsilon^{ff}_m(\underline{\phi}) \tag{5.30}$$

where $\overline{\varepsilon}_m^{bf}(\underline{\phi})$ and $\varepsilon_m^{ff}(\underline{\phi})$ are stored in the database for a set of temperature values. For local gas conditions these quantity are interpolated on-the-fly.

5.4 Assembly of Full-Spectrum k-Distributions from Narrow-Band Database

In Chapter 3, theory was developed for the calculation of full-spectrum k-distributions from the spectral absorption and emission coefficient data. The full-spectrum k-distributions required to solve the RTE in reordered g-space can be assembled very quickly from the narrow-band database for any arbitrary gas state. To develop the method, Eq. (5.5) is multiplied with the Dirac-delta function $\delta(k - \kappa_\lambda(\underline{\phi}_0))$, followed by integration over the full spectrum. Similar to the narrow-band case, this leads to

$$\frac{dI_k}{ds} = k^*(\underline{\phi}, k)[f_1(\underline{\phi}, \underline{\phi}_0, k)I_b(\phi) - I_k] + f_2(\underline{\phi}, \underline{\phi}_0, k)I_b(\underline{\phi}) \tag{5.31}$$

where

$$f_1(\underline{\phi}, \underline{\phi}_0, k) = \sum_{m=1}^{M} \left(f_{m1}(\underline{\phi}, \underline{\phi}_0, k) \frac{I_{bm}(\underline{\phi})}{I_b(\underline{\phi})} \right) \tag{5.32}$$

and

$$f_2(\underline{\phi}, \underline{\phi}_0, k) = \sum_{m=1}^{M} \left(\kappa_m^{cont}(\underline{\phi}) f_{m2}(\underline{\phi}, \underline{\phi}_0, k) \frac{I_{bm}(\underline{\phi})}{I_b(\underline{\phi})} \right) \tag{5.33}$$

Eq. (5.31) can be transformed into much smoother g-space by dividing it by the k-distribution at the reference state $f_1(\underline{\phi}_0, \underline{\phi}_0, k)$, leading to

$$\frac{dI_g}{ds} = k^*(\underline{\phi}_0, \underline{\phi}, g)[a(\underline{\phi}, \underline{\phi}_0, g)I_b(\underline{\phi}) - I_g] + b(\underline{\phi}, \underline{\phi}_0, g)I_b(\underline{\phi}) \tag{5.34}$$

with

$$I_g = I_k / f_1(\underline{\phi}_0, \underline{\phi}_0, k) \tag{5.35}$$

where $k^*(\underline{\phi}_0, \underline{\phi}, g)$ is the k vs g distribution with the absorption coefficient evaluated at local conditions $\underline{\phi}$ and the Planck function at the reference state $\underline{\phi_0}$[69], and $a(\underline{\phi}, \underline{\phi}_0, g)$ is a weight or nongray stretching function given by

$$a(\underline{\phi}, \underline{\phi}_0, g) = \frac{f_1(\underline{\phi}, \underline{\phi}_0, k)}{f_1(\underline{\phi}_0, \underline{\phi}_0, k)} = \frac{dg(\underline{\phi}, \underline{\phi}_0, k)}{dg(\underline{\phi}_0, \underline{\phi}_0, k)} \tag{5.36}$$

and

$$b(\underline{\phi}, \underline{\phi}_0, g) = \frac{f_2(\underline{\phi}, \underline{\phi}_0, k)}{f_1(\underline{\phi}_0, \underline{\phi}_0, k)} = \frac{dg_2(\underline{\phi}, \underline{\phi}_0, k)}{dg(\underline{\phi}_0, \underline{\phi}_0, k)} \tag{5.37}$$

where

$$g(\underline{\phi}, \underline{\phi}_0, k) = \int_k^\infty f_1(\underline{\phi}, \underline{\phi}_0, k)dk = \sum_{m=1}^{M} \frac{I_{bm}(\underline{\phi})}{I_b(\underline{\phi})} \int_k^\infty f_{m1}(\underline{\phi}, \underline{\phi}_0, k)$$

$$= \sum_{m=1}^{M} \frac{I_{bm}(\underline{\phi})}{I_b(\underline{\phi})} g_m(\underline{\phi}, \underline{\phi}_0, k) \tag{5.38}$$

Similarly,

$$g_2(\underline{\phi}, \underline{\phi}_0, k) = \sum_{m=1}^{M} \frac{I_{bm}(\underline{\phi})}{I_b(\underline{\phi})} \kappa_m^{cont}(\underline{\phi}) g_{m2}(\underline{\phi}, \underline{\phi}_0, k) \tag{5.39}$$

together with

$$I_b(\underline{\phi}) = \sum_{m=1}^{M} I_{bm}(\underline{\phi}) \tag{5.40}$$

Note that in Eqs. (5.36) and (5.37) the numerator and denominator are both evaluated at identical values of k, which is related to g through the following equation

$$g(\underline{\phi_0}, \underline{\phi}_0, k) = \sum_{m=1}^{M} \frac{I_{bm}(\underline{\phi})}{I_b(\underline{\phi})} g_m(\underline{\phi_0}, \underline{\phi}_0, k) \tag{5.41}$$

5.5 Application of the Database

First narrow-band k-distributions are calculated at the given state by interpolating between the stored data. This requires interpolation in three-dimensional space formed by the variables T, T_e and n_e. Since in the database all $k^{'}$-values are stored at fixed g_m-values, this requires interpolation of $k^{'}$-values for each narrow-band. A simple and efficient trilinear interpolation scheme is employed for the interpolation of data in the state space, employing a $2 \times 2 \times 2$ interpolation domain. All eight k-distributions in the interpolation domain must have the same number of points. Since, as a result of data compaction, different k-distributions may have different number of points (e.g., 32 for one and 64 for another), this may require an additional interpolation within individual k-distributions. A cubic spline interpolation scheme is employed for this purpose. Once all narrow-band k-distributions are known at a given gas state, the full-spectrum k-distribution can be assembled from the M narrow-bands using Eqs. (5.38) to (5.40). The addition in Eqs. (5.38) and (5.39) is carried out at fixed k-values. This requires another interpolation of $g_m(\underline{\phi}, k)$-values at fixed k-values for each narrow-band. Again a cubic spline scheme is utilized to carry out this interpolation.

5.6 Sample Calculations

To check the accuracy of the database a number of calculations were performed. First, the accuracy of each narrow-band k-distribution was checked by comparing narrow-band averaged absorption cross-sections $\overline{\kappa^{'}}_{\lambda m}$ and narrow-band gas column emissivities $\overline{\epsilon}_{\lambda m}$ with those obtained from line-by-line calculations using

$$\overline{\kappa^{'}}_{\lambda m} = \frac{1}{I_{bm}^c} \int_{\Delta\lambda} \kappa_\lambda^{'} I_{b\lambda}^c d\lambda = \int_0^1 k_m^{'} dg \tag{5.42}$$

$$\overline{\epsilon}_{\lambda m} = \frac{1}{I^c_{bm}} \int_{\Delta\lambda} I^c_{b\lambda}(1 - e^{-\kappa'_\lambda \Delta n L}) d\lambda = \int_0^1 (1 - e^{-k'_m \Delta n L}) dg \tag{5.43}$$

where a fixed value of $\Delta n = 5.0 \times 10^{16}$ was used. The emissivities were compared at a nominal optical thickness resulting in an emissivity of approximately 0.40-0.60, but the thickness of the layer was restricted to a maximum value of 1.0 m. Therefore, the actual emissivity value may not fall within the above specified range for all narrow-bands. The accuracy was checked for a large number of interpolated states (a total of 10000 randomly generated values of n_e, T_e and T), and the maximum error was found to be always below 0.5%. Two typical calculations (for interpolated values of n_e, T_e) are shown in Figs. 5.2 and 5.3, where the narrow-band mean absorption coefficient and emissivity of a gas column containing atomic N are compared, showing excellent agreement with line-by-line results. In Figs. 5.4 and 5.5 similar results for O are presented, indicating the same excellent accuracy as for N.

To demonstrate the accuracy of the narrow-band k-distribution database when solving atomic radiation problems in hypersonic nonequilibrium flows, an example is considered for both species, investigating a homogeneous gas slab of 1 cm thickness with typical conditions found in hypersonic shock layers. For homogeneous conditions the k-distribution method is exact and, therefore, any errors will be due entirely to the accuracy of the k-distributions as they are assembled from the database. In Fig. 5.6 the full-spectrum assembled k-distribution for atomic N and O are compared with the directly-calculated one (from line-by-line absorption coefficient data), showing very good agreement for both species. Good agreement is also found for the mixture of N and O, except at small k-values. For a mixture with overlapping bound-bound lines, the nonequilibrium Planck function cannot be described consistently between the line-by-line and the k-distribution method. The disagreement in Fig. 5.6 at small k-values stems from the neglected overlap between the two species and the inconsistency of the Planck function. For the same conditions, the RTE was solved using the tangent slab approximation. The heat flux exiting the cell is compared with that obtained from line-by-line calculations in Table 5.1, showing very good agreement for N, O, and mixture. It is clear that overlap between the two species is not significant, and causes no serious error in heat transfer calculations.

Finally, the narrow-band database was applied to the Stardust stagnation-line flow-field along with the grouping scheme developed in Chapter 4. Heat transfer results obtained from the database are compared with line-by-line results in Figs. 5.7 and 5.8. Only bound-bound radiation is compared in these calculations, demonstrating very good accuracy of the k-distribution database.

5.7 Computational Efficiency

To demonstrate the efficiency of the k-distribution method together with the databasing scheme, computational times were measured for the heat transfer calculation in the homogeneous gas slab problem discussed above. The LBL method requires calculating emission and absorption coefficients at many thousands of wavelengths and solving the RTE at each of the wavelengths. The measured cpu-times for the LBL generation of spectral data and the evaluation of the RTE are given in Table 5.2. Since time required in the LBL method directly depends on the spectral resolution at which spectral data are generated,

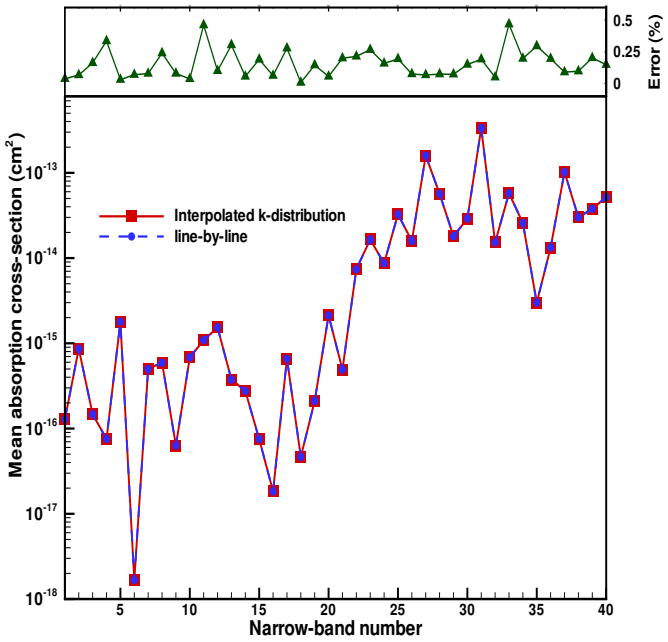

Figure 5.2. Narrow-band mean absorption coefficient of N; $n_e = 5.0 \times 10^{15}$ cm^{-3}, T_e = 10000K, T= 15000K

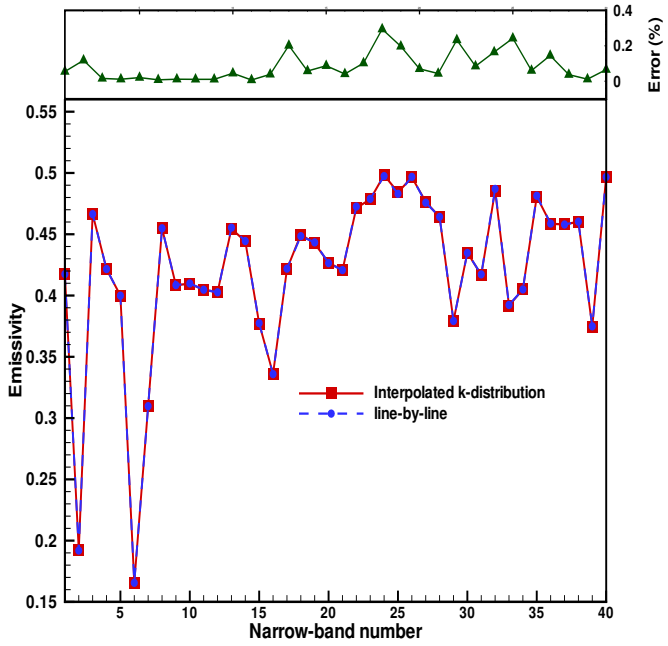

Figure 5.3. Narrow-band emissivity of N; $n_e = 5.0 \times 10^{15}$ cm^{-3}, T_e = 10000K, T= 15000K

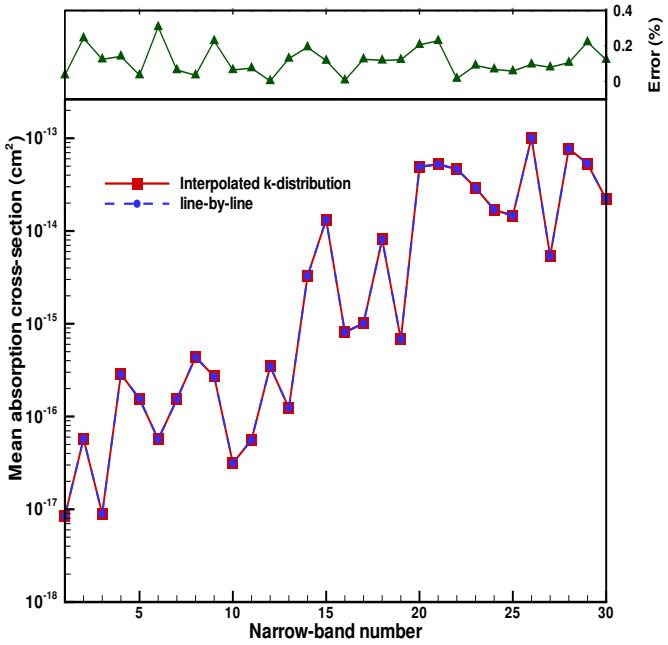

Figure 5.4. Narrow-band mean absorption coefficient of O; $n_e = 5.0 \times 10^{15}$ cm^{-3}, T_e = 10000K, T= 15000K

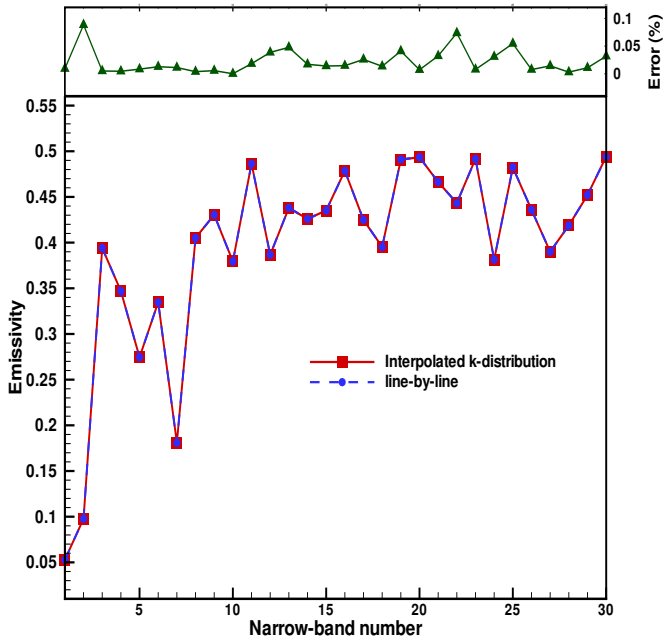

Figure 5.5. Narrow-band emissivity of O; $n_e = 5.0 \times 10^{15}$ cm^{-3}, T_e = 10000K, T= 15000K

Table 5.1. Database results for Wall heat flux, (W/cm^2)

	line-by-line	Database	error (%)
N (no continuum)	10.63	10.62	0.09
O (no continuum)	2.095	2.092	0.14
N+O+continuum	13.61	13.52	0.66

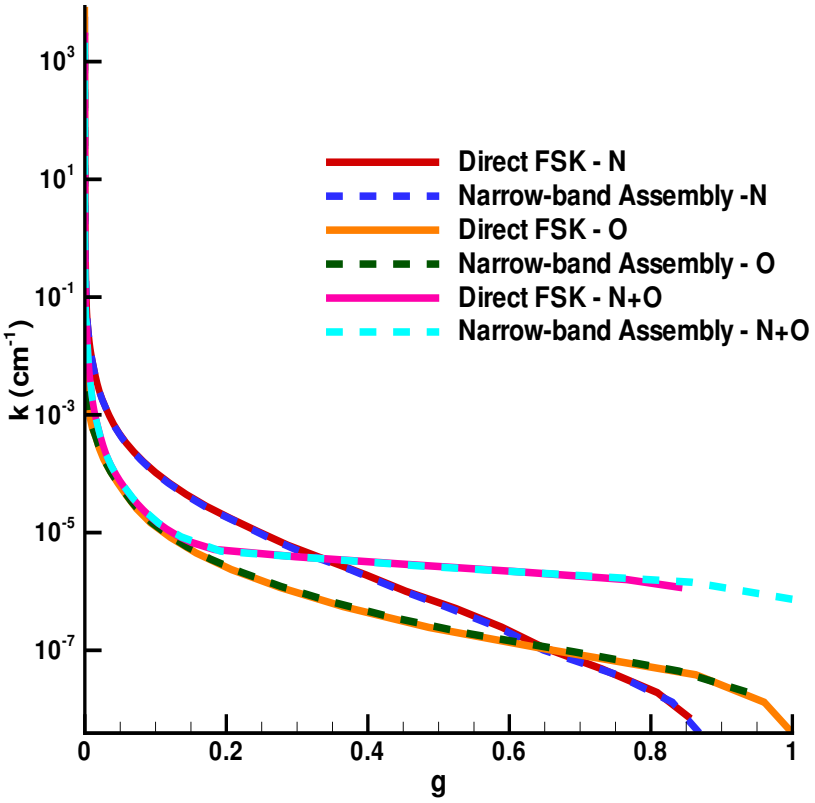

Figure 5.6. k-distribution assembly ; $n_N = 5.0 \times 10^{16}$ cm^{-3}, $n_{N^+} = 5.0 \times 10^{14}$ cm^{-3}, $n_O = 5.0 \times 10^{16}$ cm^{-3}, $n_{O^+} = 5.0 \times 10^{14}$ cm^{-3}, $n_e = 5.0 \times 10^{15}$ cm^{-3}, T$_e$ = 10000K, T= 15000K

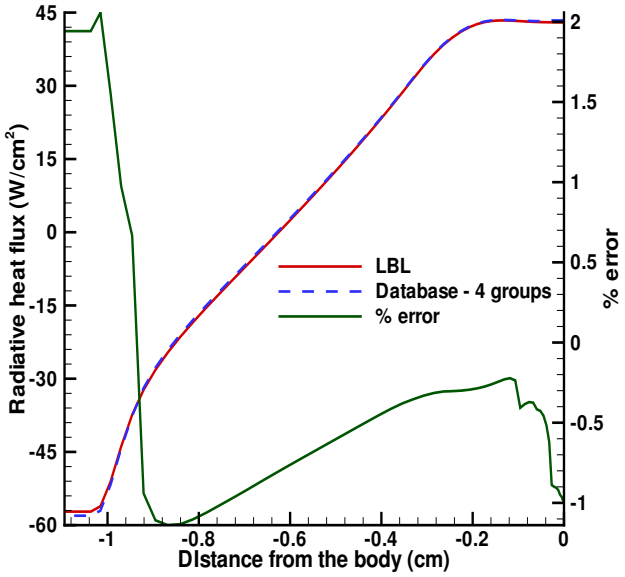

Figure 5.7. Database results for heat flux along the stagnation-line of the Stardust peak heating flow-field

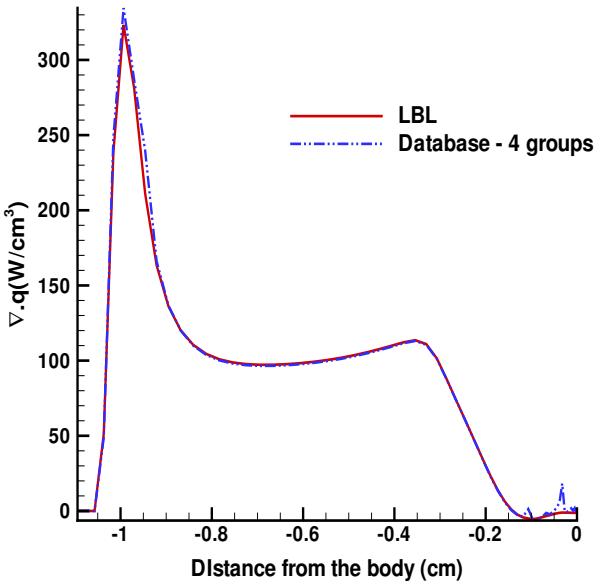

Figure 5.8. Database results for divergence of heat flux along the stagnation-line of the Stardust peak heating flow-field

results from three different resolutions are shown for comparison. In general, an atomic radiation calculation demands a resolution of at least 0.01Å for good accuracy. At coarser resolutions the accuracy of LBL results may decrease. Errors as high as $6-7\%$ in wall heat flux were observed for a resolution of 0.05Å, and this case has been included for efficiency comparison only. The correlated-k method requires calculation of spectral data (assembly of full-spectrum k-distributions from the database and calculating the a and b functions) and solving the RTE at a number of quadrature points, 128 g-points in this case.

All calculations were performed on a single Pentium-Xeon quad-core 3.0 GHz processor with cache size of 6 MB. In the k-distribution method the database reading time is not included, as this is done only once and does not need to be repeated for each flow condition. It can be observed that for this simple tangent slab solution, the generation of spectral data takes more time than solution of the RTE itself. The k-distribution method shows considerable savings in computational time for the generation of spectral data, as compared to the LBL data for all spectral resolutions. The time saving is much more significant in the evaluation of the RTE, as the RTE is evaluated at only 128 quadrature points, compared to many thousands of evaluations in the LBL method. Other, higher order RTE solution methods, for two- or three-dimensional geometries, e.g., the Spherical Harmonics and the Discrete Ordinate methods, are much more expensive than the tangent slab method, and one can expect enormous time savings when using k-distributions.

Table 5.2. Computational time comparison (ms)

	Spectral resolution	LBL data	LBL RTE	FSK data	FSK RTE
N (no continuum)	0.005Å	704	291	22	0.04
	0.01Å	352	147		
	0.05Å	70.9	29.0		
O (no continuum)	0.005Å	228	230	23	0.04
	0.01Å	114	115		
	0.05Å	23.9	22		
N+O + continuum	0.005Å	1672	611	27	0.04
	0.01Å	865	305		
	0.05Å	223	60		

Chapter 6

Conclusion and Future Work

6.1 Conclusion

The correlated-k method was developed for efficient solutions of the radiative transfer equation in a nonequilibrium flow field containing N and O species. The accuracy of the full-spectrum k-distribution method was demonstrated by comparing heat flux results with those obtained from line-by-line calculations. Reasonable accuracy, with errors below 5% in wall heat flux, was observed for the Stardust stagation line flow-field. For more extreme conditions, the full-spectrum k-distribution method was found to be somewhat less accurate. Atomic lines were separated into groups according to their absorption characteristics and electronic transitions. The agreement between line-by-line and correlated-k results is found to be excellent, if atomic lines are sorted into a small number of groups.

The full-spectrum k-distributions can be calculated from a narrow-band database, which is much more efficient than calculating them directly from line-by-line absorption coefficients. A narrow-band k-distribution database was developed for the two important monatomic species N and O. The full spectrum was broken up into 105 narrow-bands, according to the position of electronic transitions. Very accurate k-distributions were generated for each narrow-band using high-fidelity absorption cross-section data. A Gauss-Chebyshev quadrature scheme was implemented for data compaction. The accuracy of the database was checked by comparing narrow-band mean absorption coefficients and narrow-band gas column emissivities with those obtained from line-by-line calculations, showing excellent accuracy. Finally, the database was applied to generate full-spectrum k-distributions and a number of heat transfer calculation were performed for both species, demonstrating that full-spectrum k-distributions can be assembled accurately and efficiently from the narrow-band database. Computational times for the assembly of full-spectrum k-distributions from the database were compared with the directly calculated ones for various cases of spectral resolutions, showing significant reduction in the calculation time for all cases. The k-distribution method is vastly more efficient than the line-by-line method. In the line-by-line method approximately one quarter million evaluations of RTE must be performed, while in the correlated-k method an efficient Gauss-quadrature scheme allowed very fast evaluation of the RTE, requiring at most 128 integration points. The efficiency of the full-spectrum k-distribution method can be matched by gray

calculations only, which are very inaccurate for optically thick atomic lines.

6.2 Future Work

In the present work full-spectrum *k*-distribution models were developed for atomic N and O. These two species dominate the radiative heat transfer in the shock-layer over a nonablating body in air. For aerocapture in other atmospheres, similar models needs to be developed for other species, including C, H etc. Molecular radiation is known to be significant in many reentry situations. CN is one of the most important radiating specie in the atmospheres of Titan, Mars and Venus. Even for Earth reentry conditions, significant amount of CN may be present in ablation products. In the present work it was found that the overlap between N and O lines is not significant. This may not be true for other species, particularly molecular-bands which are known to overlap each other. It is not straightforward to apply the FSK method to gas mixtures. For gas-mixtures with overlapping bands, mixing schemes for the *k*-distributions needs to be developed. As *k*-distributions do not retain any information of spectral location of absorption lines in various band systems, it is impossible to combine the individual *k*-distributions exactly. Solovjov and Webb [95] and Modest and Riazzi [93] have proposed a number of approximate mixing models for the *k*-distributions, with the later being more accurate than the former. Mixing of individual *k*-distributions can be carried out either on a full-spectrum basis or narrow-band basis. A number of approaches, like MSFSCK and MGFSCK, needs to be investigated to develop an accurate *k*-distribution method for a mixture.

Appendix

Table 1. Details of electronic states of N

i	n	E,cm^{-1}	g	States included
N atom, E_∞ = 117,345 cm^{-1}				
1	2	0	4	$2p^3\ ^4S$
2	2	19228	10	$2p^3\ ^2D$
3	2	28840	6	$2p^3\ ^2P$
4	3	83337	12	$3s\ ^4P$
5	3	86193	6	$3s\ ^2P$
6	3	95276	36	$3p\ ^4D$, $3p\ ^4P$, $3p\ ^4S$
7	3	96793	18	$3p\ ^2S$, $3p\ ^2D$, $3p\ ^2P$
8	4	103862	18	$4s\ ^4P$, $4s\ ^2P$
9	3	104857	60	$3d\ ^4F$, $3d\ ^4P$, $3d\ ^4D$
10	3	104902	30	$3d\ ^2P$, $3d\ ^2F$, $3d\ ^2D$
11	4	107082	54	$4p\ ^2S$, $4p\ ^4D$, $4p\ ^4P$, $4p\ ^2D$, $4p\ ^4S$, $4p\ ^2P$
12	5	110021	18	$5s\ ^4P$, $5s\ ^2P$
13	4	110315	90	$4d\ ^2P$, $4d\ ^4F$, $4d\ ^4D$, $4d\ ^2F$, $4d\ ^4P$, $4d\ ^2D$
14	4	110486	126	$4f\ ^4D$, $4f\ ^4F$, $4f\ ^4G$, $4f\ ^2D$, $4f\ ^2F$, $4f\ ^2G$
15	5	111363	54	$5p\ ^4S$, $5p\ ^4P$, $5p\ ^4D$, $5p\ ^2S$, $5p\ ^2P$, $5p\ ^2D$
16	5	112851	90	$5d\ ^2P$, $5d\ ^4F$, $5d\ ^4D$, $5d\ ^2F$, $5d\ ^4P$, $5d\ ^2D$
17	5	112929	288	$5f\ ^4D$, $5f\ ^4F$, $5f\ ^4G$, $5f\ ^2D$, $5f\ ^2F$, $5f\ ^2G$, $5g\ ^4F$
18	6	114298	648	$n = 6$
19	7	115107	882	$n = 7$
20	8	115631	1152	$n = 8$
21	9	115991	1458	$n = 9$
22	10	116248	1800	$n = 10$

Table 2. Details of electronic states of O

O atom, $E_\infty = 109{,}837\ \mathrm{cm}^{-1}$				
1	2	78	9	$2p^4\ ^3P$
2	2	15868	5	$2p^4\ ^1D$
3	2	33792	1	$2p^4\ ^1S$
4	3	73768	5	$3s\ ^5S$
5	3	76795	3	$3s\ ^3S$
6	3	86629	15	$3p\ ^5P$
7	3	88631	9	$3p\ ^3P$
8	4	95757	8	$4s\ ^5S$, $4s\ ^3S$
9	3	97445	40	$3d\ ^5D$, $3d\ ^3D$
10	4	99313	24	$4p\ ^5P$, $4p\ ^3P$
11	5	102227	8	$5s\ ^5S$, $5s\ ^3S$
12	4	102881	96	$4d\ ^5D$, $4f\ ^5F$, $4d\ ^3D$, $4f\ ^3F$
13	5	103869	24	$5p\ ^5P$, $5p^3P$
14	5	105394	168	$5d\ ^5D$, $5f\ ^5F$, $5g\ ^5G$, $5d\ ^3D$, $5f\ ^3F$, $5g\ ^3F$
15	6	106639	288	$n = 6$
16	7	107583	392	$n = 7$
17	8	108117	512	$n = 8$
18	9	108478	648	$n = 9$
19	10	108734	800	$n = 10$

Table 3. Narrow-band details

Nb	Id	U	L	λ_{start}(Å)	λ_{end}(Å)	I^c_{bi}(W/cm^{2}sr)
1	0	0	0	580.8	607.5	0.43102E + 12
2	0	0	0	607.5	653.8	0.55591E + 12
3	0	0	0	653.8	800.0	0.90288E + 12
4	2	19	1	800.0	852.2	0.16238E + 12
5	2	19	1	852.2	890.0	0.89998E + 11
6	0	0	0	890.0	911.1	0.42459E + 11
7	2	19	2	911.1	980.0	0.10930E + 12
8	2	11	1	980.0	995.0	0.19031E + 11
9	2	19	2	995.0	1005.0	0.11912E + 11
10	0	0	0	1005.0	1020.0	0.16794E + 11
11	2	9	1	1020.0	1035.0	0.15604E + 11
12	0	0	0	1035.0	1100.0	0.56107E + 11
13	1	12	2	1100.0	1103.0	0.22036E + 10
14	0	0	0	1103.0	1129.9	0.18471E + 11
15	1	5	1	1129.9	1137.0	0.45336E + 10
16	3	10(12)[1]	2(1)	1137.0	1171.5	0.20079E + 11
17	1	8	2	1171.5	1195.0	0.12073E + 11
18	1	4	1	1195.0	1205.0	0.47870E + 10
19	0	0	0	1205.0	1216.0	0.50413E + 10
20	2	19	3	1216.0	1220.0	0.17773E + 10
21	0	0	0	1220.0	1226.0	0.26119E + 10
22	1	12	3	1226.0	1238.0	0.50363E + 10
23	0	0	0	1238.0	1241.0	0.12213E + 10
24	1	7	2	1241.0	1272.0	0.11798E + 11
25	0	0	0	1272.0	1292.0	0.68810E + 10
26	2	5	1	1292.0	1308.0	0.51335E + 10
27	1	10	3	1308.0	1322.0	0.42412E + 10
28	0	0	0	1322.0	1324.0	0.58771E + 09
29	1	8	3	1324.0	1332.0	0.23070E + 10
30	0	0	0	1332.0	1410.0	0.19257E + 11
31	1	7	3	1410.0	1414.0	0.84883E + 09
32	0	0	0	1414.0	1480.0	0.12424E + 11
33	1	5	2	1480.0	1500.0	0.32443E + 10
34	0	0	0	1500.0	1740.0	0.26333E + 11
35	1	5	3	1740.0	1750.0	0.73616E + 09
36	0	0	0	1750.0	3925.0	0.30493E + 11
37	2	10	4	3925.0	3975.0	0.61944E + 08
38	0	0	0	3975.0	4080.0	0.11812E + 09
39	1	14	5	4080.0	4120.0	0.41127E + 08
40	1	11	4	4120.0	4308.0	0.16893E + 09
41	0	0	0	4308.0	4330.0	0.17436E + 08
42	2	10	5	4330.0	4380.0	0.38022E + 08
43	1	22	7	4380.0	4400.0	0.14610E + 08
44	0	0	0	4400.0	4900.0	0.27792E + 09
45	1	11	5	4900.0	5185.0	0.10454E + 09
46	0	0	0	5185.0	5190.0	0.15853E + 07
47	1	16	7	5190.0	5210.0	0.62654E + 07
48	0	0	0	5210.0	5270.0	0.18092E + 08
49	3	11(14)	5(6)	5270.0	5475.0	0.54650E + 08
50	0	0	0	5475.0	5800.0	0.68263E + 08
51	1	16	6	5800.0	5880.0	0.14030E + 08
52	0	0	0	5880.0	6000.0	0.19338E + 08
53	2	14	7	6000.0	6100.0	0.14699E + 08

Nb	Id	U	L	λ_{start}(Å)	λ_{end}(Å)	I^c_{bi}(W/m^{2}sr)
54	2	12	6	6100.0	6200.0	$0.13542E+08$
55	2	19	11	6200.0	6300.0	$0.12493E+08$
56	2	11	6	6400.0	6500.0	$0.10672E+08$
57	0	0	0	6500.0	6625.0	$0.12237E+08$
58	1	12	6	6625.0	6675.0	$0.45795E+07$
59	0	0	0	6675.0	6900.0	$0.18628E+08$
60	3	12(12)	6(7)	6900.0	7050.0	$0.10828E+08$
61	0	0	0	7050.0	7100.0	$0.33597E+07$
62	2	19	12	7100.0	7200.0	$0.63754E+07$
63	2	11	7	7200.0	7300.0	$0.59476E+07$
64	0	0	0	7300.0	7410.0	$0.60888E+07$
65	1	6	4	7410.0	7480.0	$0.36455E+07$
66	0	0	0	7480.0	7750.0	$0.12578E+08$
67	2	6	4	7750.0	7800.0	$0.20961E+07$
68	0	0	0	7800.0	7900.0	$0.39964E+07$
69	2	19	11	7900.0	7975.0	$0.28354E+07$
70	2	11	7	7975.0	8025.0	$0.18175E+07$
71	0	0	0	8025.0	8175.0	$0.51260E+07$
72	3	6(19)	4(11)	8175.0	8275.0	$0.31647E+07$
73	0	0	0	8275.0	8400.0	$0.36964E+07$
74	2	7	5	8400.0	8500.0	$0.27652E+07$
75	0	0	0	8500.0	8530.0	$0.79824E+06$
76	1	7	5	8530.0	8672.0	$0.35944E+07$
77	1	6	4	8672.0	8760.0	$0.20839E+07$
78	0	0	0	8760.0	8775.0	$0.34486E+06$
79	2	19	12	8775.0	8875.0	$0.22255E+07$
80	0	0	0	8875.0	9010.0	$0.28125E+07$
81	1	10	7	9010.0	9038.0	$0.55731E+06$
82	1	14	7	9038.0	9059.0	$0.41235E+06$
83	1	10	7	9059.0	9075.0	$0.31098E+06$
84	0	0	0	9075.0	9200.0	$0.23378E+07$
85	2	9	6	9200.0	9300.0	$0.17591E+07$
86	0	0	0	9300.0	9350.0	$0.84464E+06$
87	3	7(19)	5(12)	9350.0	9475.0	$0.20156E+07$
88	0	0	0	9475.0	9770.0	$0.42641E+07$
89	1	9	6	9770.0	10570.0	$0.88262E+07$
90	0	0	0	10570.0	10580.0	$0.90059E+05$
91	1	22	14	10580.0	10610.0	$0.26764E+06$
92	1	9	6	10610.0	10780.0	$0.14475E+07$
93	0	0	0	10780.0	11200.0	$0.31260E+07$
94	3	8(9)	6(7)	11200.0	11295.0	$0.62865E+06$
95	3	8(8)	6(6)	11295.0	11350.0	$0.35204E+06$
96	0	0	0	11350.0	11550.0	$0.12109E+07$
97	1	6	5	11550.0	11680.0	$0.73256E+06$
98	0	0	0	11680.0	12120.0	$0.21998E+07$
99	1	8	6	12120.0	12293.0	$0.76055E+06$
100	1	9	6	12293.0	12300.0	$0.29657E+05$
101	1	8	6	12300.0	12312.0	$0.50644E+05$
102	1	9	6	12312.0	12412.0	$0.41259E+06$
103	1	10	7	12412.0	12600.0	$0.73218E+06$
104	0	0	0	12600.0	13100.0	$0.17030E+07$
105	2	8	7	13100.0	13200.0	$0.30292E+06$

* Numbers in bracket are for atomic O for bands having contribution from both species

Table 4. Datapoints for the narrow-band database

Parameter	Data points	Number
$T(K)$	5000 – 35000	12
$T_e(K)$	5000 – 25000	16
$n_e(\mathrm{cm}^{-3})$	$1.0 \times 10^{13} - 7.0 \times 10^{17}$	50
Narrow-bands	N, O and Continuum	105

Translation temperature T, electron temperature T_e and electron density n_e used in the database are chosen according to a power-law distribution as

$$\Delta(x^\beta) = [(x_{max})^\beta - (x_{min})^\beta]/(N_{pt} - 1) \tag{1}$$

$$x^i = [(x_{min})^\beta - i\Delta(x^\beta)]^{1/\beta},\ i = 1, 2, ..., N_{pt} \tag{2}$$

where $x = T, T_e$ and n_e; and β =0.1 is taken. This distribution places more points near smaller values of electron number density and the two temperatures.

Bibliography

[1] Braun, R. D. and Manning, R. M., 2005, "Mars Exploration Entry, Descent and Landing Challenges", *IEEEAC Paper No. 0076*.

[2] Olynick, D. R., Henline, W. D., Hartung-Chambers, L., and Candler, G. V., 1995, "Comparison of Coupled Radiative Flow Solutions with Project Fire II flight Data", *Journal of Thermophysics and Heat Transfer*, **9**(4), pp. 586–594.

[3] Osawa, H., Matsuyama, S., Ohnishi, N., and Sawada, K., 2006, "Comparative Computation of Radiative Heating Evnironment for Hyugens Probe Entry Flight", *AIAA Paper No. 2006-3772*, 9th AIAA/ASME Joint Thermophysics and Heat Transfer Conference, San Francisco, California.

[4] Anderson, J. D., 1969, "An Engineering Survey of Radiating Shock Layers", *AIAA Journal*, **7**, pp. 1665–1675.

[5] Park, Chul, 2004, "Stagnation-Point Radiation for Apollo 4", *Journal of Thermophysics and Heat Transfer*, **18**, pp. 349–357.

[6] Sutton, Kenneth, "Heating Analysis for the Pioneer Venus Multi-Probe Mission", *NASA-TM-X-72001*.

[7] Florence, D.E., 1981, "Aerothermodynamic Design Feasibility of a Mars Aerocapture/Aeromaneuver Vehicle", *AIAA Paper No. 81-0350*.

[8] Park, C., Howe, J.T., Jaffe, R.L., and Candler, G. V., 1994, "Review of Chemical-Kinetic Problems of Future NASA Missions, II: Mars Entries", *Journal of Thermophysics and Heat Transfer*, **8**, pp. 9–23.

[9] Kudiyavtsev, N. N., Kuznetsova, L.A., and Surzhikov, S.T., "Kinetics and Nonequilibrium Radiation of CO_2/N_2 Shock Waves", *Journal of Thermophysics and Heat Transfer*, **19**.

[10] Tauber, M. E. and Wakefield, R. M., 1971, "Heating Environment and Protection during Jupiter Entry", *Journal of Spacecraft and Rockets*, **8**, pp. 630–636.

[11] Matsuyama, S., Shimogonya, Y., Ohnishi, N., Sawada, K., and Sasoh, A., 2005, "Numerical Simulation of Galileo Probe Entry Flowfield with Radiation and Ablation", *Journal of Thermophysics and Heat Transfer*, **19**, pp. 28–35.

[12] Tiwari, S. N. and Subramanian, S. V., "Influence of Nonequilibrium Radiation and Shape Change on Aerothermal Environment of a Jovian Entry Body", *NASA-CR-3432*.

[13] Hollis, B. R., Wright, M. J., Olejniczak, J., Takashima, N., Sutton, K., and Prabhu, D., 2004, "Preliminary Convective-Radiative Heating Environments for a Neptune Aerocapture Mission", *AIAA Paper No. 2004-5177*, AIAA Atmospheric Flight Mechanics Conference and Exhibit, Providence, Rhode Island.

[14] Tiwari, S.N. and Chow, H., "Impotance of Radiative Heating for a Titan Aerocapture Mission", *NASA-CR-16999*.

[15] Olejniczak, J., Wright, M., Prabhu, D., Takashima, N., Hollis, B., and Zoby, E. V., 2003, "An Analysis of the Radiative Heating Environment for Aerocapture at Titan", *AIAA Paper No. 2003-4953*, 39th AIAA/ASME/SAE/ASEE Joint Propulsion Conference and Exhibit, Huntsville, Alabama.

[16] Olynick, D., Chen, Y.-K., and Tauber, M. E., 1999, "Aerothermodynamics of the Stardust Sample Return Capsule", *Journal of Spacecraft and Rockets*, **36**(3), pp. 442–462.

[17] Gupta, R. N., 2000, "Aerothermodynamic Analysis of Stardust Sample Return Capsule with Coupled Radiation and Ablation", *Journal of Spacecraft and Rockets*, **37**, pp. 507–514.

[18] Park, C., "Calculation of Stagnation-Point Heating Rates Associated with Stardust Vehicle", *Journal of Spacecraft and Rockets*, **44**.

[19] Liu, Y., Prabhu, D., Trumble, K. A., Saunders, D., and Jenniskens, P., 2008, "Radiation modelling for rhe reentry of the Stardust sample return capsule", *AIAA Paper No. 2008-1213*, 46th AIAA Aerospace Sciences Meeting and Exhibit, Reno, Nevada.

[20] Wright, M. J., Bose, D., and Olejniczak, J., 2005, "The Impact of Flowfield-Radiation Coupling on Aeroheating for Tital Aerocapture", *Journal of Thermophysics and Heat Transfer*, **19**(1), pp. 17–27.

[21] Olejniczak, J., Prabhu, D., Bose, D., and Wright, M. J., 2004, "Aeroheating Analysis for the Afterbody of a Titan Probe", *AIAA Paper No. 2004-0486*, 42nd AIAA Aerospace Sciences Meeting and Exhibit, Reno, Nevada.

[22] Bose, D., Wright, M. J., Bogdanoff, D., Raiche, G., and Allen, G., 2006, "Modeling and Experiment Assessment of CN Radiation Behind a Strong Shock Wave", *Journal of Thermophysics and Heat Transfer*, **20**(2), pp. 220–230.

[23] Hollis, B. R., Striepe, S. A., Wright, M. J., Bose, D., Sutton, K., and Takashima, N., 2005, "Prediction of the Aerothermodynamic Evnironment of the Huygens Probe", *AIAA Paper No. 2005-4816*, 38th AIAA Thermophysics Conference, Toronto, Ontario.

[24] Sakai, T. and Sawada, K., "Calculation of Nonequilibrium Radiation from a Blunt-Body Shock Layer", *Journal of Thermophysics and Heat Transfer*, **15**.

[25] Hoshizaki, R. B. and Lasher, L. E., 1967, "Convective and Radiative Heat Transfer to an Ablating Body", *AIAA Paper No. 67-327*, New Orleans, LA.

[26] Coleman, W. D., 1968, "A Study of the Effect of Environmental and Ablator Performance Uncertainities on Heat Shielding Requirements for Blunt and Slender Hyperbolic-Entry Vehicles", *AIAA Paper No. 68-154*, New York.

[27] Sutton, K. and Falanga, R. A., 1973, "Stagnation Region Radiative Heating with Steady-State Ablation during Venus Entry", *Journal of Spacecraft and Rockets*, **10**, pp. 155–157.

[28] Moss, J. N., Zoby, E. V., Sutton, K., and Anderson, E. C., 1978, "Aerothermal Environment for the Pioneer Venus Multiprobe Mission", *Aerodynamic Heating and Thermal Protection Systems, Progress in Astronautics and Aeronautics, edited by L. S. Fletcher, AIAA, New York*, **59**, pp. 3–26.

[29] Moss, J. N. and Simmonds, A. L., 1982, "Galileo Probe Forebody Flow-Field Prediction", *AIAA Paper No. 82-0874*.

[30] Raiche, G. A. and Driver, D. M., 2004, "Shock Layer Optical Attanuation and Emission spectraoscopy measurements during arc jet testing with ablating models", *AIAA Paper No. 2004-*, 42nd AIA Aerospace Sciences Meeting and Exhibit, Reno, Nevada.

[31] Park, C., Raiche, G. A., and Driver, D. M., 2004, "Radiation of Spalled Particles in Shock Layers", *Journal of Thermophysics and Heat Transfer*, **18**(4), pp. 519–526.

[32] Goulard, R., 1961, "The Coupling of Radiation and Convection in Detached Shock Layers", *Journal of Quantitative Spectroscopy and Radiative Transfer*, **1**, pp. 249–257.

[33] Johnston, C. O., Gnoffo, P. A., and Sutton, K, 2008, "The Influence of Ablation on Radiative Heating for Earth Entry", *AIAA Paper No. 2008-4107*, 40th Thermophysics Conference, Seattle, Washington.

[34] Nicolet, W. E., "User's Manual for RAD/EQUIL/1973, A Genral Purpose Radiation Transport Program", *NASA CR-132470*.

[35] Whiting, E., Park, C., Liu, Y., Arnold, J., and Paterson, J., December 1996, *NEQAIR96, Nonequilibrium and Equilibrium Radiative Transport and Spectra Program: User's Manual*, NASA/Ames Research Center, Moffett Field, CA 94035-1000, NASA Reference Publication 1389.

[36] Wiese, W.L., Smith, M.W., and Glennon, B.M., "Atomic Transition Probabilities, Vol. 1, Hydrogen through Neon, NSRDS-NBS 4, National Bureau of Standards".

[37] Arnold, J.O., Whiting, E.E., and Lyle, G.C., 1969, "Line by Line Calculation of Spectra from Diatomic Molecules and Atoms Assuming a Voight Line Profile", *Journal of Quantitative Spectroscopy and Radiative Transfer*, **9**, pp. 775–798.

[38] Carlson, L.A. and Gally, T.A., 1992, "Nonequilibrium Chemical and Radiation Coupling, Part I:Theory and Models", *Journal of Thermophysics and Heat Transfer*, **6**, pp. 385–391.

[39] Gally, T.A., Carlson, L.A., and Green, D., 1993, "Flowfield Coupled Excitation and Radiation Model for Nonequilibrium Reacting Flows", *Journal of Thermophysics and Heat Transfer*, **7**, pp. 285–293.

[40] Johnston, C. O., "Nonequilibrium Shock-Layer Radiative Heating for Earth and Titan Entry", *Ph.D. Dissertation, Virginia Polytechnic Institute and State University, 2006.*

[41] Hartung, L. C., "Predicting Radiative Heat Transfer in Thermochemical Nonequilibrium Flow Fields: Theory and User's Manual for the LORAN Code", *NASA TM 4564*.

[42] Hartung, L. C., 1992, "Development of a Nonequilibrium Radiative Prediction Method for Coupled Flowfield Solutions", *Journal of Thermophysics and Heat Transfer*, **6**, pp. 618–625.

[43] Sohn, I., Bansal, A., Levin, D. A., and Modest, M. F., 2009, "Advanced Radiation Calculations of Hypersonic Reentry Flows Using Efficient Databasing Schemes", *Journal of Thermophysics and Heat Transfer*, submitted for publication.

[44] Bose, D. and Wright, M. J., 2004, "View-Factor-Based Radiation Transport in a Hypersonic Shock Layer", *Journal of Thermophysics and Heat Transfer*, **18**(4), pp. 553–555.

[45] Hartung, L. C. and Hassan, H. A., 1993, "Radiation TransportAround Axisymmetric Blunt Body Vehicles Using a Modified Differential Approximation", *Journal of Thermophysics and Heat Transfer*, **7**, pp. 220–227.

[46] Modest, M. F., 1989, "The Modified Differential Approximation for Radiative Transfer in General Three-Dimensional Media", *Journal of Thermophysics and Heat Transfer*, **3**(3), pp. 283–288.

[47] T., Surzhikov S., Rouzaud, O., and Soubrie, T., "Prediction of Non-Equilibrium and Equilibrium Radiation for Re-Entry Conditions", *AIAA Paper No. 2006-1188*, 44th AIAA Aerospace Sciences Meeting and Exhibit 9 - 12 January 2006, Reno, Nevada.

[48] Wang, A. and Modest, M. F., 2007, "Spectral Monte Carlo Models for Nongray Radiation Analyses in Inhomogeneous Participating Media", *International Journal of Heat and Mass Transfer*, **50**, pp. 3877–3889.

[49] Ozawa, T., Modest, M. F., and Levin, D. A., 2008, "Spectral Module for Photon Monte Carlo Calculations in Hypersonic Nonequilibrium Radiation", *ASME Journal of Heat Transfer*, (submitted).

[50] Ozawa, T., Wang, A., Levin, D. A., and Modest, M. F., 2009, "Development of a Coupled DSMC – Particle Photon Monte Carlo Method for Simulating Atomic Radiation in Hypersonic Reentry Flows", *Journal of Thermophysics and Heat Transfer*, (to be submitted).

[51] Feldick, A. M., Giegel, J., and Modest, M. F., July 2009, "A Spectrally Accurate Tightly–Coupled 2-D Axisymmetric Photon Monte-Carlo RTE Solver For Hypersonic Entry Flows", *ASME Summer Heat Transfer Conference, San Fransisco, California, Paper No. HT2009-88241*.

[52] Modest, M. F., 2003, *Radiative Heat Transfer*, Academic Press, New York, 2nd ed.

[53] Yoshikawa, K. K. and Wick, B. H., "Radiative Heat Transfer During Atmospheric Entry at Parabolic Velocity", *TN-D-1074,NASA*.

[54] Howe, J. T. and Viegas, J. R., "Solution of the Ionized Radiating Shock Layer, Including Re-Absorption and Foreign species Effects and Stagnation Region Heat Transfer", *TR-R-159,NASA*.

[55] Hoshizaki, H. and Wilson, K. H., 1967, "Convective and Radiative Heat Transfer During Superorbital entry", *AIAA Journal*, **5**, pp. 25–35.

[56] Olstad, W. B., "Stagnation-point Solution for an Inviscid Radiating Shock Layer", *Proceedings of the 1965 Heat Transfer and Fluid Mechanics Institute, Stanford University Press, Stanford, California*.

[57] Biberman, L. M., 1964, "Radiation Heating Under Hypersonic Flow", *Astronautica Acta*, **10**, pp. 238–253.

[58] Patch, R. W., Shackleford, W. L., and Penner, S. S., 1962, "Approximate Spectral Absorption Coefficient Calculations for Electronic Band Systems Belonging to Diatomic Molecules", *Journal of Quantitative Spectroscopy and Radiative Transfer*, **2**, pp. 263–271.

[59] Hartung-Chambers, L., 1994, "Predicting Radiative Heat Transfer in Thermochemical Nonequilibrium Flow Fields", *NASA Technical Memorandum 4564*.

[60] Johnston, C. O., Hollis, B. R., and Sutton, K., 2006, "Radiative Heating Methodology for the Huygens Probe", *AIAA Paper No. 2006-3426*, 9th AIAA/ASME Joint Thermophysics and Heat Transfer Conference, San Francisco, California.

[61] Sakai, T., Sawada, K., and Park, C., 1997, "Assesment of Planck Rosseland Gray model for Radiating Shock Layer", *AIAA Paper No. 97-2560*.

[62] Hermann, W. and Schade, E., 1971, "Radiative Energy Balance in Cylendrical Nitrogen Arcs", *Journal of Quantitative Spectroscopy and Radiative Transfer*, **12**, pp. 1257–1282.

[63] Lacis, A. A. and Oinas, V., 1991, "A Description of the Correlated-k Distribution Method for Modeling Nongray Gaseous Absorption, Thermal Emission, and Multiple Scattering in Vertically Inhomogeneous Atmospheres", *Journal of Geophysical Research*, **96**(D5), pp. 9027–9063.

[64] Goody, R. M. and Yung, Y. L., 1989, *Atmospheric Radiation – Theoretical Basis*, Oxford University Press, New York, 2nd ed.

[65] Rivière, P., Soufiani, A., and Taine, J., 1992, "Correlated-*k* and Fictitious Gas Methods for H_2O near 2.7 μm", *Journal of Quantitative Spectroscopy and Radiative Transfer*, **48**, pp. 187–203.

[66] Rivière, P., Soufiani, A., and Taine, J., 1995, "Correlated-*k* and Fictitious Gas Model for H_2O Infrared Radiation in the Voigt Regime", *Journal of Quantitative Spectroscopy and Radiative Transfer*, **53**, pp. 335–346.

[67] Rivière, P., Scutaru, D., Soufiani, A., and Taine, J., 1994, "A New $c-k$ Data Base Suitable from 300 to 2500 K for Spectrally Correlated Radiative Transfer in CO_2–H_2O Transparent Gas Mixtures", In *Tenth International Heat Transfer Conference*, Taylor & Francis, pp. 129–134.

[68] Modest, M. F. and Zhang, H., 2002, "The Full-Spectrum Correlated-*k* Distribution For Thermal Radiation from Molecular Gas–Particulate Mixtures", *ASME Journal of Heat Transfer*, **124**(1), pp. 30–38.

[69] Modest, M. F., 2003, "Narrow-band and full-spectrum *k*-distributions for radiative heat transfer—correlated-*k* vs. scaling approximation", *Journal of Quantitative Spectroscopy and Radiative Transfer*, **76**(1), pp. 69–83.

[70] Hottel, H. C. and Sarofim, A. F., 1967, *Radiative Transfer*, McGraw-Hill, New York.

[71] Modest, M. F., 1991, "The Weighted-Sum-of-Gray-Gases Model for Arbitrary Solution Methods in Radiative Transfer", *ASME Journal of Heat Transfer*, **113**(3), pp. 650–656.

[72] Denison, M. K. and Webb, B. W., 1993, "A Spectral Line Based Weighted-Sum-of-Gray-gases Model for Arbitrary RTE Solvers", *ASME Journal of Heat Transfer*, **115**, pp. 1004–1012.

[73] Denison, M. K. and Webb, B. W., 1995, "The Spectral-Line-Based Weighted-Sum-of-Gray-Gases Model in Nonisothermal Nonhomogeneous Media", *ASME Journal of Heat Transfer*, **117**, pp. 359–365.

[74] Rivière, P., Soufiani, A., Perrin, M. Y., Riad, H., and A., Gleizes, 1996, "Air Mixture Radiative Property Modelling in the Temperature Range 10000-40000K", *Journal of Quantitative Spectroscopy and Radiative Transfer*, **56**, pp. 29–45.

[75] Pierrot, L., Rivière, Ph., Soufiani, A., and Taine, J., 1999, "A Fictitious-gas-based Absorption Distribution Function Global Model for Radiative Transfer in Hot Gases", *Journal of Quantitative Spectroscopy and Radiative Transfer*, **62**, pp. 609–624.

[76] Zhang, H. and Modest, M. F., 2002, "A Multi-Scale Full-Spectrum Correlated-*k* Distribution For Radiative Heat Transfer in Inhomogeneous Gas Mixtures", *Journal of Quantitative Spectroscopy and Radiative Transfer*, **73**(2–5), pp. 349–360.

[77] Wang, L. and Modest, M. F., 2005, "Narrow-Band Based Multi-Scale Full-Spectrum *k*-Distribution Method for Radiative Transfer in Inhomogeneous Gas Mixtures", *ASME Journal of Heat Transfer*, **127**, pp. 740–748.

[78] Wang, L. and Modest, M. F., 2005, "Multi-Scale Full-Spectrum *k*-Distribution Method for Radiative Transfer in Inhomogeneous Gas Mixtures with Wall Emission", In Webb, B. and Modest, M. F., eds., *Proceedings of the 2005 ASME Summer Heat Transfer Conference*, San Francisco, CA.

[79] Zhang, H. and Modest, M. F., 2003, "Scalable Multi-Group Full-Spectrum Correlated-*k* Distributions For Radiative Heat Transfer", *ASME Journal of Heat Transfer*, **125**(3), pp. 454–461.

[80] Zhang, H. and Modest, M. F., 2003, "Multi-Group Full-Spectrum *k*-Distribution Database For Water Vapor Mixtures in Radiative Transfer Calculations", *International Journal of Heat and Mass Transfer*, **46**(19), pp. 3593–3603.

[81] Wang, L. and Modest, M. F., 2005, "A Hybrid Multi-Scale Full-Spectrum *k*-Distribution Method for Radiative Transfer in Inhomogeneous Gas Mixtures", In *Proceedings of IMECE 2005*, Orlando, FL, ASME.

[82] Pal, G., Modest, M. F., and Wang, L., 2008, "Hybrid Full-Spectrum Correlated k-Distribution Method for Radiative Transfer in Strongly Nonhomogeneous Gas Mixtures", *ASME Journal of Heat Transfer*, **130**, pp. 082701–1–082701–8.

[83] Bose, D., McCorkle, E., Thompson, C., and Grinstead, J., 2008, "Analysis and Model Validation of Shock Layer Radiation in Air", *AIAA Paper No. 2008-1246*, 46th AIAA Aerospace Sciences Meeting and Exhibit, Reno, Nevada.

[84] Park, C., 1990, *Nonequilibrium Hypersonic Aerothermodynamics*, Wiley, New York.

[85] McCorkle, E., Bose, D., Hash, D. B., and Hassan, H. A., 2009, "Improved Modeling of Shock Layer Radiation in Air", *AIAA Paper No. 2009-1028*, 47th AIAA Aerospace Sciences Meeting Including The New Horizons Forum and Aerospace Exposition, Orlando, Florida.

[86] Chauveau, S., Perrin, M.Y., Riviere, P., and Soufiani, A., 2002, "Contributions of diatomic molecular electronic systems to heated air radiation", *Journal of Quantitative Spectroscopy and Radiative Transfer*, **72**, pp. 503–530.

[87] Chauveau, S., Deron, C., Perrin, M.Y., Riviere, P., and Soufiani, A., 2003, "Radiative Transfer in LTE Air Plasmas for Temperatures up to 15,000 K", *Journal of Quantitative Spectroscopy and Radiative Transfer*, **73**, pp. 113–130.

[88] Park, C., 1969, "Theoretical Population Inversion in a Decaying Nitrogen Plasma Column", *AIAA Paper No. 69-48*.

[89] Sharma, S., 1996, "Modeling of Nonequilibrium Radiation Phenomena: An Assessment", *Journal of Thermophysics and Heat Transfer*, **10**, pp. 385–396.

[90] Kunc, J.A. and Soon, W.H., 1989, "Collisional-Radiative Nonequilibrium in Partially Ionized Atomic Nitrogen", *Physical Review A*, **40**, pp. 5822–5843.

[91] Soon, W.H. and Kunc, J.A., 1990, "Thermal Nonequilibrium in Partially Ionized Atomic Oxygen", *Physical Review A*, **41**, pp. 825–843.

[92] Modest, M. F. and Singh, V., 2005, "Engineering correlations for full spectrum *k*-distribution of H_2O from the HITEMP spectroscopic databank", *Journal of Quantitative Spectroscopy and Radiative Transfer*, **93**, pp. 263–271.

[93] Modest, M. F. and Riazzi, R. J., 2004, "Assembly of Full-Spectrum *k*-Distributions from a Narrow-Band Database; Effects of Mixing Gases, Gases and Nongray Absorbing Particles, and Mixtures with Nongray Scatterers in Nongray Enclosures", *Journal of Quantitative Spectroscopy and Radiative Transfer*, **90**(2), pp. 169–189.

[94] Wang, A. and Modest, M. F., 2004, "High-Accuracy, Compact Database of Narrow-Band *k*-Distributions for Water Vapor and Carbon Dioxide", In Mengüç, M. P. and Selçuk, N., eds., *Proceedings of the ICHMT 4th International Symposium on Radiative Transfer*, Istanbul, Turkey.

[95] Solovjov, V. and Webb, B. W., 2000, "SLW Modeling of Radiative Transfer in Multicomponent Gas Mixtures", *Journal of Quantitative Spectroscopy and Radiative Transfer*, **65**, pp. 655–672.